ISSN 1560-3547, Regular and Chaotic Dynamics, 2015, Vol. 20, No. 3, pp. 345–382. © Pleiades Publishing, Ltd., 2015.

Plate Falling in a Fluid: Regular and Chaotic Dynamics of Finite-dimensional Models

Sergey P. Kuznetsov*

Kotel'nikov's Institute of Radio Engineering and Electronics of RAS, Saratov Branch, ul. Zelenaya 38, Saratov, 410019 Russia

Received December 22, 2014; accepted January 16, 2015

Abstract—Results are reviewed concerning the planar problem of a plate falling in a resisting medium studied with models based on ordinary differential equations for a small number of dynamical variables. A unified model is introduced to conduct a comparative analysis of the dynamical behaviors of models of Kozlov, Tanabe – Kaneko, Belmonte – Eisenberg – Moses and Andersen – Pesavento – Wang using common dimensionless variables and parameters. It is shown that the overall structure of the parameter spaces for the different models manifests certain similarities caused by the same inherent symmetry and by the universal nature of the phenomena involved in nonlinear dynamics (fixed points, limit cycles, attractors, and bifurcations).

MSC2010 numbers: 34C15, 76D99, 37E99

DOI: 10.1134/S1560354715030090

Keywords: body motion in a fluid, oscillations, autorotation, flutter, attractor, bifurcation, chaos, Lyapunov exponent

The article is dedicated to the 65th anniversary of Academician Valery V. Kozlov, with respect and admiration for his contribution to the problem under review

INTRODUCTION

The dynamics of a flat sheet falling in a resisting medium are the content of one of the classical problems in hydrodynamics and aerodynamics, the analysis of which goes back to Maxwell, Kelvin, Kirchhoff, Joukovsky, relating to the 19th and early 20th century [1–6].

Elementary experiments show that various kinds of dynamical behavior can occur depending on parameters and initial conditions:

- simple steady fall,
- shaking from side to side, which can be regular or irregular (flutter),
- tumbling (autorotation), regular or irregular.

Naturally, there is the problem of finding conditions for implementation of these regimes, of understanding their nature in the context of the theory of dynamical systems, and exploring bifurcations leading to the occurrence of certain types of motion.

A full and correct approach to the description of motion of a body in a viscous incompressible fluid implies the investigation of the time-varying velocity field in the surrounding region based on the Navier – Stokes equations [7–12], which requires complicated resource-intensive computations. Data obtained in this way are obviously not easy for comprehension, and, given the expected diversity of types of dynamics depending on many parameters, still need qualitative interpretation on the physical level for understanding.

This is a translation of the paper "Motion of a falling card in a fluid: Finite-dimensional models, complex phenomena, and nonlinear dynamics", *Nelin. Din.*, 2015, vol. 11, no. 1, pp. 3–49, previously published only in Russian.

*E-mail: spkuz@yandex.ru

A reasonable initial step to simplifying the analysis is to restrict consideration to the plane problem. This means that only two spatial coordinates X and Y are significant, while the third one Z is regarded as irrelevant: the system is assumed to be extended in the Z-direction; there are no motions along this axis and no dependences of variables on Z.

Next, one can turn to an approximate description of the problem with models in the form of ordinary differential equations for a small number of variables, i. e., to dynamical systems with a relatively small dimension of the phase space. Although the validity of such an approach is not so obvious, it has a great advantage in that within this framework one can use powerful conceptual tools of modern dynamical systems theory for analysis of the problem. In particular, well-established and proven methods of computational studies and data processing such as graphical presentation of portraits of attractors [13–15], charts of dynamical regimes in the parameter space [15–17, 56, 57], computation of Lyapunov exponents [14, 15, 18], and bifurcation analysis [19] may be applied in the explorations.

An important motivation for finite-dimensional description is the fact that governing equations for generalized coordinates and velocities of the solid body moving in an ideal nonviscous incompressible fluid can be decoupled from the field equations of the fluid itself. The corresponding equations were derived and studied by Kirchhoff [2, 7–10, 20, 21]. The effect of fluid motion on the body only modifies the inertial properties; instead of usual masses and moments of inertia, one has to deal in the equations with added masses and moments of inertia due to the contribution of the fluid motions in adjacent space regions. In the plane problem, forces acting on the body from the fluid are determined by the circulation of the velocity field around the body profile, and in the case of an ideal fluid the circulation appears simply as a constant parameter; in particular, it may be zero.

Actually, the Kirchhoff equations relate to a situation of excluded losses of mechanical energy, and the corresponding dynamical system is conservative. Then, many properties of dynamical behavior of the falling body which are significant from the practical point of view remain outside the scope of consideration as they are associated with dissipation. It relates, e. g., to steady fall regimes and to sustained regular or chaotic oscillations and rotations [20, 21]. To study such motions, it seems natural to take account of dissipation in a phenomenological way by introducing appropriately chosen additional terms into the Kirchhoff equations [22–28].

This review is devoted to models for the plane hydrodynamic problem based on ordinary differential equations and to comparison of these models. One of the main goals is to flesh out the picture of dynamical phenomena relating to this problem using illustrative material obtained in computations. Relationship of this material with results based on the Navier – Stokes equations [29–32], as well as with experimental data [33–38], will not be considered. Also, we do not discuss situations of motion of bodies in resisting media beyond the plane problem [36–38] and generalizations, including control of the body motion in a fluid [39–43, 58, 59].

In Section 1 we discuss the plane problem of a body of elliptic profile falling in an ideal fluid and present equations of motion taking into account the effect of added masses. In Section 2 we deal with a special case where the gravity is compensated by the buoyancy force, and reduce the dynamics to a pendulum-type equation with the sine nonlinearity. In Section 3 we consider the Kozlov model derived from a conservative system taking into account only the viscous friction forces and the torque resistance force linear in the generalized velocities. We discuss a special case where the model is integrable and reduces to the pendulum equation with damping, and present an analysis of stability loss for a steady uniform fall, which may lead to autorotation. In Section 4 we consider a modification of the model, in which the gravity is excluded, constant circulation is assumed, and constant torque of external force is applied to the body. We show that in this situation chaotic dynamics occur which are associated with the strange attractor of Lorenz type. Section 5 is devoted to a model introduced by Tanabe and Kaneko, which takes into account the drag forces and lift force due to the presence of circulation, expressed via the dynamical variables using the postulate of Kutta – Joukovsky – Chaplygin. Taking into account the critical remarks in the literature concerning this model, we consider ways of its modification. We present an approximate analysis of a nonstandard bifurcation accompanying the transition from the steady fall to the oscillatory regime in the Tanabe – Kaneko model. In Section 6 we discuss the model advanced by Belmonte, Eisenberg and Moses, in which, unlike the Tanabe – Kaneko model, the resistance force and torque depend quadratically on the generalized velocities. In Section 7 we consider a model elaborated by Andersen, Pesavento, and Wang who introduce empirically chosen dissipative terms and circulation in the Kirchhoff equations fitting the data of numerical solution

of the Navier – Stokes equations. In Section 8 we formulate generalized equations which allow a comparative analysis of the dynamical behavior of all the mentioned models using the same set of dimensionless variables and parameters.

1. PLANE PROBLEM OF A BODY FALLING IN AN IDEAL FLUID

We will use two coordinate systems: a laboratory frame (X, Y), where the position of the center of mass of the body is given by the Cartesian coordinates X and Y, and a moving frame (x, y), the axes of which are fixed in the body (Fig. 1).

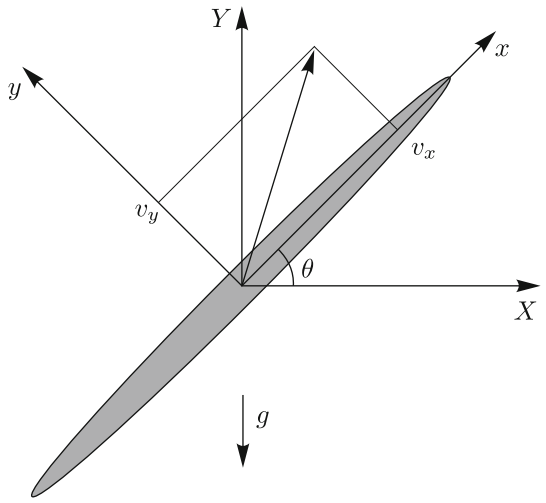

Fig. 1. Laboratory and moving coordinate frames in the plane problem of a body falling in a resisting medium

Let us start with the problem of a body falling in an ideal incompressible nonviscous fluid.

Taking into account the inertial properties of the body and its environment, the kinetic energy may be written as

$$T = \frac{1}{2}(m + m_x)v_x^2 + \frac{1}{2}(m + m_y)v_y^2 + \frac{1}{2}(I + J)\dot{\theta}^2, \tag{1.1}$$

where v_x and v_y are the velocity components referred to the moving frame, $\dot{\theta}$ is the angular velocity, the time derivative of the angular coordinate of the body, m is the mass and I is the moment of inertia of the body. The additional terms m_x, m_y, and J take into account the added masses due to involvement of surrounding fluid volumes in the motion. We assume that the body has density ρ_s, and the fluid has density ρ_f. Since we deal with the plane problem, the densities are defined as mass per unit area in a cross-section.

According to classic hydrodynamics [7–12], for a body moving in an ideal nonviscous fluid there are no resistance forces (the d'Alembert – Euler paradox), but forces acting on the body appear due to nonzero circulation Γ of the velocity field around a contour enclosing the body (Joukovsky theorem). The value of Γ does not depend on a particular choice of the contour. Moreover, Γ remains constant in time (the Kelvin – Helmholtz theorem) and is determined by initial conditions for the velocity field in the fluid. The components of the force are $f_x = -\rho_f \Gamma v_y$ and $f_y = \rho_f \Gamma v_x$.

In the presence of gravity characterized by the gravitational acceleration g reduced due to the buoyancy, the equations for the velocity components and the angular variable read

$$\begin{aligned}
(m + m_x)\dot{v}_x &= (m + m_y)v_y\dot{\theta} - \rho_f \Gamma v_y - mg(1 - \rho_f \rho_s^{-1}) \sin\theta, \\
(m + m_y)\dot{v}_y &= -(m + m_x)v_x\dot{\theta} + \rho_f \Gamma v_x - mg(1 - \rho_f \rho_s^{-1}) \cos\theta, \\
(I + J)\ddot{\theta} &= (m_x - m_y)v_x v_y.
\end{aligned} \tag{1.2}$$

The coordinates of the center of mass in the laboratory frame evolve in time as determined by the equations

$$\dot{X} = v_x \cos\theta - v_y \sin\theta, \quad \dot{Y} = v_x \sin\theta + v_y \cos\theta. \tag{1.3}$$

For the body of elliptic profile with semiaxes a and b the mass and the moment of inertia are

$$m = \pi\rho_s ab, \quad I = \frac{1}{4}\pi\rho_s ab(a^2 + b^2), \tag{1.4}$$

and the added masses and the moment of inertia in an ideal nonviscous fluid are expressed as [9]

$$m_x = \pi\rho_f b^2, \quad m_y = \pi\rho_f a^2, \quad J = \frac{1}{8}\pi\rho_f (a^2 - b^2)^2. \tag{1.5}$$

Substitution of these relations into (1.2) yields

$$\begin{aligned} A\dot{v}_x &= Bv_y\dot{\theta} - \rho\beta^{-1}\frac{\Gamma v_y}{\pi a^2} - g(1-\rho)\sin\theta, \\ B\dot{v}_y &= -Av_x\dot{\theta} + \rho\beta^{-1}\frac{\Gamma v_x}{\pi a^2} - g(1-\rho)\cos\theta, \\ Q\ddot{\theta} &= a^{-2}(A-B)v_x v_y, \end{aligned} \tag{1.6}$$

where shortened notation for the coefficients is used:

$$A = 1 + \rho\beta, \quad B = 1 + \rho\beta^{-1}, \quad Q = \frac{1}{4}(1+\beta^2) + \frac{1}{8}\rho\beta^{-1}(1-\beta^2)^2. \tag{1.7}$$

Here $\rho = \rho_f/\rho_s$ is the ratio of densities for the fluid and the body, and $\beta = b/a$ is the ratio of the semiaxes of the ellipse.

In some cases it is convenient to rescale the velocity components additionally as $u = v_x/a$, $v = v_y/a$ and rewrite equations (1.6) in the form

$$\begin{aligned} A\dot{u} &= Bv\dot{\theta} - \rho\beta^{-1}\frac{\Gamma v}{\pi a^2} - ga^{-1}(1-\rho)\sin\theta, \\ B\dot{v} &= -Au\dot{\theta} + \rho\beta^{-1}\frac{\Gamma u}{\pi a^2} - ga^{-1}(1-\rho)\cos\theta, \\ Q\ddot{\theta} &= (A-B)uv. \end{aligned} \tag{1.8}$$

2. CONSERVATIVE DYNAMICS WITHOUT GRAVITY

We first consider the case of equal density of the fluid and the body, $\rho = 1$. Then the gravity effect is excluded by the buoyancy, and Eqs. (1.8) take the form

$$\begin{aligned} A\dot{u} &= Bv\dot{\theta} - \Gamma' v, \\ B\dot{v} &= -Au\dot{\theta} + \Gamma' u, \\ Q\ddot{\theta} &= (A-B)uv, \end{aligned} \tag{2.1}$$

where $\Gamma' = \Gamma/\pi a^2\beta = \Gamma/\pi ab$. The substitution

$$u = RA^{-1}\cos\varphi, \quad v = -RB^{-1}\sin\varphi \tag{2.2}$$

transforms the equations to

$$\begin{aligned} \dot{R} &= \Gamma' R\frac{A-B}{AB}\sin\varphi\cos\varphi, \\ \dot{\varphi} &= \dot{\theta} - \Gamma'(A^{-1}\cos^2\varphi + B^{-1}\sin^2\varphi), \\ \ddot{\theta} &= -\frac{A-B}{ABQ}R^2\sin\varphi\cos\varphi. \end{aligned} \tag{2.3}$$

Here φ is the angle between the principal axis of the elliptic profile and the translational velocity of the body, and θ is the angle of inclination of the body's principal axis measured in the laboratory frame.

If we multiply the first equation by R and add to the third equation, the right-hand side vanishes, and then a combination under the derivative is an integral of motion:

$$D^2 = R^2 + 2\Gamma' Q\dot{\theta} = \text{const}. \tag{2.4}$$

Expressing R from this relation, we obtain a single equation for the angular variable φ:

$$\ddot{\varphi} = \frac{A-B}{2QAB}\left(-D^2 + \Gamma'^2 Q\frac{A+B}{2AB} - \Gamma'^2 Q\frac{A-B}{2AB}\cos 2\varphi\right)\sin 2\varphi. \tag{2.5}$$

In the case of zero circulation $\Gamma' = 0$ Eqs. (2.1) for the variables u, v, $w = \dot{\theta}$ take the form [7]

$$A\dot{u} = Bvw, \quad B\dot{v} = -Auw, \quad Q\dot{w} = (A-B)uv. \tag{2.6}$$

According to (2.4), the integral of motion in this case is R, which in view of the added masses is equivalent to conservation of translational momentum of the body. From the second equation of (2.3) we see that $\dot{\varphi} = \dot{\theta}$, so without loss of generality, in this case one can identify φ and θ. (This is so because an origin for θ can be chosen arbitrarily due to spatial isotropy of the problem without gravity.) Then, for θ we get the relation

$$\ddot{\theta} + \frac{(A-B)}{ABQ}R^2\cos\theta\sin\theta = 0, \tag{2.7}$$

which coincides precisely with the pendulum equation written for the doubled angular variable $\vartheta = 2\theta$ (due to the identity $\sin\theta\cos\theta = \frac{1}{2}\sin 2\theta$) [7]. Figure 2 shows the phase portrait for this equation in the plane $(\theta, \dot{\theta})$. Due to the fact that θ is a cyclic variable, the configuration is 2π-periodic. Therefore, the phase portrait can be thought of as placed on the surface of a cylinder resulting from rolling a plane band of width 2π into a tube and gluing the vertical edges together.

The fixed points $\theta = \pi/2$ and $\theta = 3\pi/2$ are stable centers corresponding to the uniform motion of the body, with the wide side forwards. The fixed points $\theta = 0$ and $\theta = \pi$ represent unstable saddle states corresponding to the uniform motion of the profile, with the edge forwards. On the phase portrait one can see the separatrix containing the saddle points. The orbits inside the separatrix correspond to oscillatory motions around the centers, while the rotational motions are represented by curves outside the separatrix. The motion precisely along the separatrices can be obtained by setting the initial conditions $\theta_0 = \frac{\pi}{2}$, $w_0 = \pm R\sqrt{\frac{B-A}{ABQ}}$.

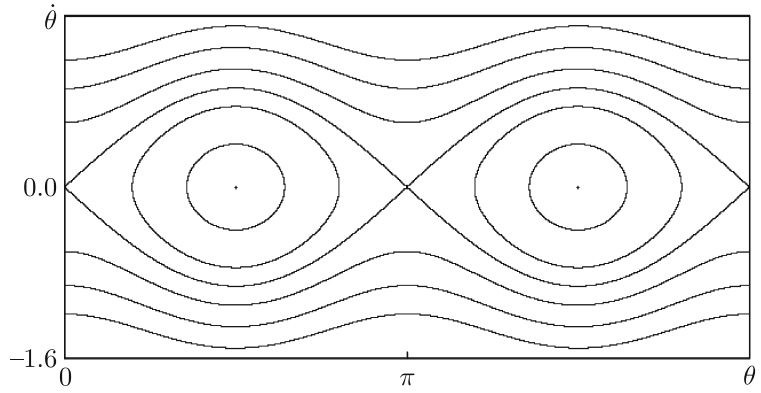

Fig. 2. Phase portrait of equation (2.7) with $\beta = 0.25$, $R = 1$.

The diagrams in Fig. 3 illustrate motions of the body in real space as obtained from joint numerical integration of Eqs. (2.6) and equations for coordinates of the center of mass: $\dot{X} = u\cos\theta - v\sin\theta$, $\dot{Y} = u\sin\theta + v\cos\theta$. The top picture relates to a stable steady motion of the body

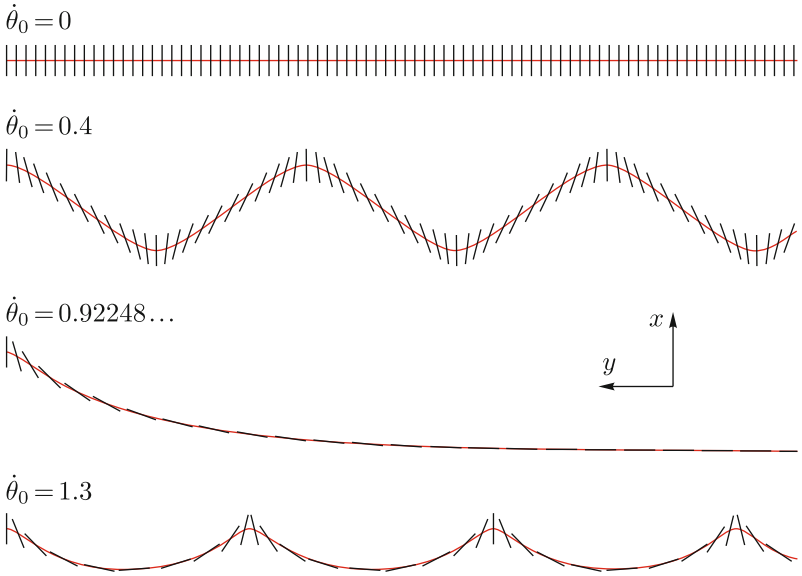

Fig. 3. Motion of the body of elliptic profile in an ideal fluid without circulation at $\beta = 0.25$, $R = 1$. The positions of the principal axis of the elliptic profile are shown at successive time instants. The initial angle is $\theta_0 = \pi/2$, and the initial angular velocities are listed in the inscriptions.

associated with the fixed point (center) on the phase portrait. The other pictures illustrate, from the top down, the oscillatory side-to-side motion, the motion along the separatrix asymptotically approaching an unstable stationary state, and rotational motion where the body tumbles in the course of time evolution.

In the presence of nonzero circulation, the variables φ (the angle between the velocity vector and the principal axis of the ellipse) and θ (the angle of inclination of the profile in the laboratory frame) must be distinguished as they behave differently. Figure 4 shows the phase portrait for the value of the integral of motion $D = 1$ and circulation $\Gamma = 0.4$ on the plane of variables φ and $w = \dot\theta$. Although the form of trajectories differs from that of Fig. 2, the topological structure remains the same. Observe again the stable centers and the unstable saddles at the separatrix dividing the plane into regions of oscillatory motions represented by closed curves and regions of rotational motions associated with curves going from side to side of the rectangle. Analysis of motions in space in the case of nonzero circulation shows that the oscillatory or rotational motions of the body take place against the background of a gradual displacement of the center of mass around some midpoint (Fig. 5).

The quite simple and descriptive results presented above provide a good starting point for further analysis of motions in the presence of dissipation and gravity. This is analogous to a productive approach in the theory of oscillations, when a conservative oscillator is considered as

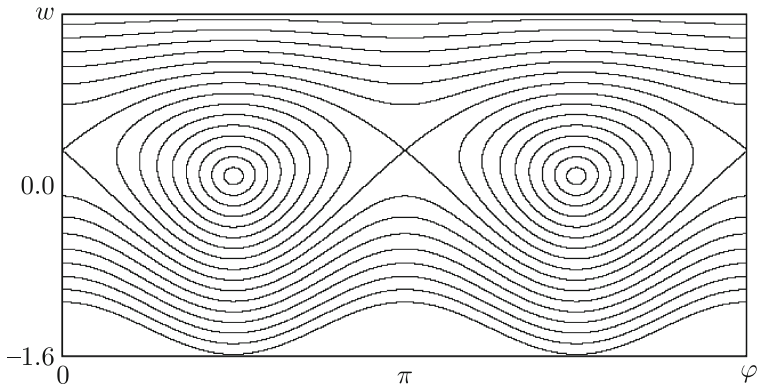

Fig. 4. Phase portrait of the dynamics in the case of nonzero circulation, $\Gamma = 0.4$, $\beta = 0.25$, $D = 1$.

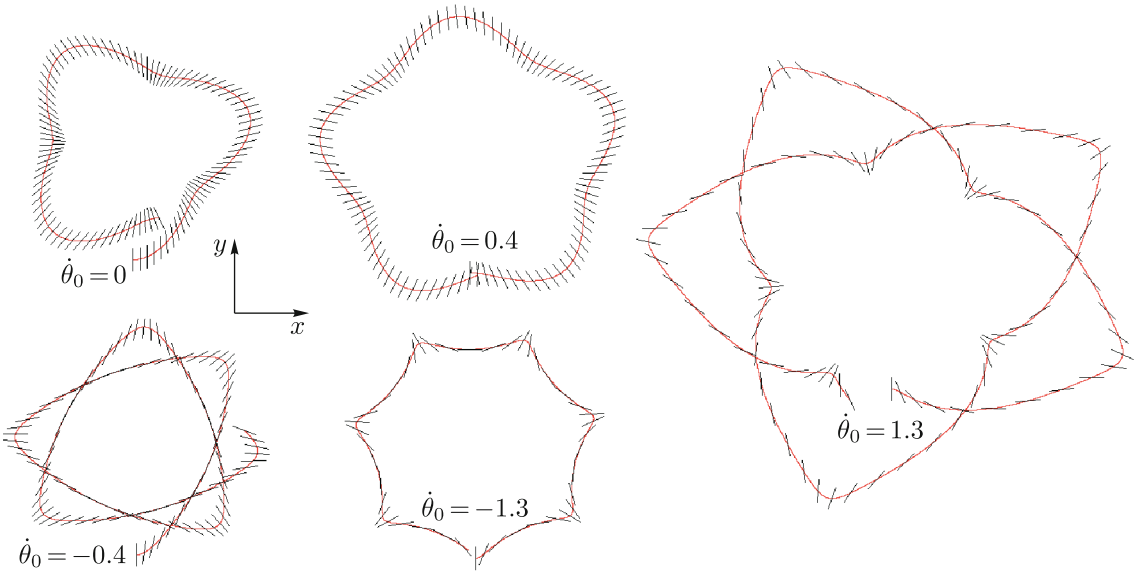

Fig. 5. Diagrams illustrating the motion of a body of elliptical profile in an ideal fluid for the case of nonzero circulation $\Gamma = 1$ for $\beta = 0.25$ with different initial conditions.

a paradigmatic model for subsequent modifications involving, say, damping oscillations or self-oscillations corresponding to attracting closed orbits, the limit cycles [44, 45].

For systems whose states are represented on the phase cylinder, the oscillation theory distinguishes limit cycles of the first kind as closed loops on the cylinder surface, and those of the second kind, as the curves bypassing around the cylinder. In the context of the problem of a body falling in a fluid, the first case corresponds to sustained oscillations from side to side (flutter), and the second to the fall with tumbling (autorotation).

3. KOZLOV MODEL: FALLING BODY WITH VISCOUS FRICTION

The simplest model of a body falling in a fluid with gravity and viscous friction is based on the assumption that the circulation is zero, and the added dissipative terms are proportional to the translation velocity components and to the angular velocity [22].

When taking into account the viscous friction force, it seems natural to proceed from the well-known Stokes formula [7, 9–11]. For steady motion of a sphere of radius R_0 in a viscous medium with velocity V it reads

$$F = -6\pi\eta R_0 V, \tag{3.1}$$

where η is the viscosity coefficient. In many cases it is useful to represent it as a product of the fluid density and the kinematical viscosity: $\eta = \rho_f \nu$. For the body in the form of ellipsoid with semiaxes a, b, c there is a generalization [7], the same formula, but with modified geometric parameter R_*. In the case of motions along the a-axis it is

$$\frac{1}{R_*} = \int\limits_0^\infty \frac{3(\lambda + 2a^2)d\lambda}{8\sqrt{(\lambda + a^2)^3(\lambda + b^2)(\lambda + c^2)}}. \tag{3.2}$$

In the context of the three-dimensional problem of a body falling in a fluid this solution could be used for bodies in the form of “pancake” (disc of elliptical shape) in a limit case of high viscosity. However, in a two-dimensional problem it is not applicable according to the so-called Stokes paradox [7, 10, 11]. Nevertheless, from the physical point of view, since in reality the geometric dimensions of the body are limited in all three dimensions, it seems appropriate to

assume that the components of the viscous force are represented by expressions similar in structure to the Stokes formula, namely, as

$$F_x = -c_1 \eta a v_x, \quad F_y = -c_2 \eta a v_y, \tag{3.3}$$

and the viscous resisting torque for rotational motion is

$$M_\theta = -c_3 \eta a^3 \dot\theta, \tag{3.4}$$

where $c_{1,2,3}$ are some coefficients. Taking these forces into account corresponds to adding terms in (1.8) which are the derivatives of the Rayleigh function [22]

$$R = \frac{1}{2} c_1 \eta a v_x^2 + \frac{1}{2} c_2 \eta a v_y^2 + \frac{1}{2} c_3 \eta a^3 \dot\theta^2 \tag{3.5}$$

with respect to the respective generalized velocities. Then, instead of Eqs. (1.8) we write

$$\begin{aligned} A\dot u &= -\mu_1 u + Bv\dot\theta - P\sin\theta, \\ B\dot v &= -\mu_2 v - Au\dot\theta - P\cos\theta, \\ Q\ddot\theta &= -\mu_3 \dot\theta + (A-B)uv, \end{aligned} \tag{3.6}$$

where $\mu_{1,2,3} = \eta\beta^{-1}\pi^{-1}a^{-1}c_{1,2,3} = \rho\beta^{-1}\pi^{-1}\nu a^{-1}c_{1,2,3} = \rho\beta^{-1}k_{1,2,3}$, $P = ga^{-1}(1-\rho)$.

If the ratio of the friction coefficients along two principal axes of the elliptical profile is equal to the ratio of the effective masses, Eq. (3.6) can be integrated analytically. Indeed, let $\mu_1 = A\mu$, $\mu_2 = B\mu$, and $z = (Au + iBv)e^{-\mu t - i\theta}$. Then, from the first two equations of (3.6) we obtain $\dot z = -iPe^{\mu t}$ and $z = -iP\int e^{\mu t}\,dt$. Thus, we have

$$\begin{aligned} Au &= -P\mu^{-1}\left(1 - e^{-\mu t}\right)\sin\theta + ce^{-\mu t}\sin(\theta+\alpha), \\ Bv &= -P\mu^{-1}\left(1 - e^{-\mu t}\right)\cos\theta + ce^{-\mu t}\cos(\theta+\alpha), \end{aligned} \tag{3.7}$$

where c and α are constants determined by initial conditions. At asymptotically large t the velocities satisfy the relations

$$u = -PA^{-1}\mu^{-1}\cos\theta, \quad v = -PB^{-1}\mu^{-1}\sin\theta. \tag{3.8}$$

The angular variable in this asymptotic regime will be governed by the third equation of (3.6), where one has to substitute (3.8). Then it takes the form of the damped pendulum equation

$$\ddot\theta = -\frac{\mu_3}{Q}\dot\theta + \frac{(A-B)P^2}{QAB\mu^2}\sin\theta\cos\theta. \tag{3.9}$$

(Note an obvious correspondence of this equation to Eq. (2.3) for the conservative case.) If the initial conditions are chosen in such a way that the body motion is originally rotational, then over time it transforms, first, to oscillation without tumbling, and then the oscillations decay, and finally the steady fall occurs, which corresponds to a stable fixed point

$$u = 0, \quad v = -P/\mu_2, \quad w = \dot\theta = 0, \quad \theta = 0. \tag{3.10}$$

(One more stationary solution $\theta = \pi$ is equivalent in properties to (3.13), as there are two orientations of the falling body: with one or the other wide side down.)

Kozlov also studied the stability of the stationary solutions of (3.10) for arbitrary friction coefficients $\mu_{1,2,3}$.

Let us add small perturbations to the solution (3.10). Then, expanding to first order, we obtain from (3.5) the linearized equations for the perturbations marked with a tilde:

$$\begin{aligned} A\dot{\widetilde u} &= -\mu_1\widetilde u - BP\mu_2^{-1}\widetilde w - P\widetilde\theta, \\ B\dot{\widetilde v} &= -\mu_2\widetilde v, \\ Q\dot{\widetilde w} &= -\mu_3\widetilde w + (B-A)P\mu_2^{-1}\widetilde u, \\ \dot{\widetilde\theta} &= \widetilde w. \end{aligned} \tag{3.11}$$

The exponential substitution $\widetilde{u},\ \widetilde{v},\ \widetilde{w},\ \widetilde{\theta} \sim e^{st}$ yields the characteristic equation

$$\left(s+\frac{\mu_2}{B}\right)\left[s^3+\left(\frac{\mu_1}{A}+\frac{\mu_3}{Q}\right)s^2+\frac{\mu_1\mu_2^2\mu_3+(B-A)BP^2}{\mu_2^2AQ}s+\frac{(B-A)P^2}{\mu_2AQ}\right]=0. \tag{3.12}$$

Among four roots of this equation there is a trivial one, $s_0=-\mu_2/B$, and the remaining three are the roots of the cubic equation with real coefficients. Stability loss occurs when a real part of a pair of complex conjugate roots vanishes. This condition can be derived if we look for a solution of the cubic equation in the form $s=i\zeta$ that leads to the relations

$$\left[-\zeta^2+\frac{\mu_1\mu_2^2\mu_3+(B-A)BP^2}{\mu_2^2AQ}\right]\zeta=0,\quad \left(\frac{\mu_1}{A}+\frac{\mu_3}{Q}\right)\zeta^2-\frac{(B-A)P^2}{\mu_2AQ}=0. \tag{3.13}$$

Assuming $\zeta\neq 0$, we have

$$\frac{\mu_2}{B}=\left(\frac{\mu_1}{A}+\frac{\mu_3}{Q}\right)\left[1+\frac{\mu_1\mu_2^2\mu_3}{(B-A)BP^2}\right]. \tag{3.14}$$

(Note that in the integrable case $\mu_2/B=\mu_1/A$ the equality is impossible: while $\mu_{1,2,3}>0$ and $B>A$, the right-hand side in (3.14) is obviously greater than the left-hand side, so the fixed point (3.10) is always stable.)

To pass from the elliptic profile to a thin plate, it is natural to consider the limit $\beta=b/a\to 0$.[1)] Of interest is the case when simultaneously the density ratio approaches zero too, while the value $r=\rho/\beta$ remains fixed. This ratio is regarded as a relevant parameter of the model. Rescaling time, velocities, and friction coefficients

$$u=u'\sqrt{ga^{-1}},\quad v=v'\sqrt{ga^{-1}},\quad t=t'\sqrt{g^{-1}a},\quad k_{1,2,3}=k'_{1,2,3}\sqrt{ga^{-1}}, \tag{3.15}$$

and omitting primes for brevity, we arrive at the equations

$$\begin{aligned}
&\dot u=-rk_1u+(1+r)v\dot\theta-\sin\theta,\\
&(1+r)\dot v=-rk_2v-u\dot\theta-\cos\theta,\\
&\left(\frac14+\frac18r\right)\ddot\theta=-rk_3\dot\theta-ruv.
\end{aligned} \tag{3.16}$$

Equations (3.16) correspond to the form (3.6) with $A=1$, $B=1+r$, $Q=\frac14+\frac18r$, $P=1$, $\mu_{1,2,3}=rk_{1,2,3}$, and all the above results can be easily reformulated in terms of them. In particular, this concerns the pendulum-like equation with damping (3.9) in the integrable case with $k_1=k_2/(1+r)$. Also, the condition of stability loss for the fixed point corresponding to the steady fall (3.14) can be rewritten as

$$\frac{k_2}{1+r}=\left(k_1+\frac{8k_3}{2+r}\right)\left(1+\frac{r^3k_1k_2^2k_3}{1+r}\right). \tag{3.17}$$

Figure 6 illustrates the dynamics of the model (3.16) in the phase plane $(\theta,\,\dot\theta)$ or, as may be interpreted, on the phase cylinder. In diagram (a) the motion, which is initially rotational, transforms to damping oscillations, and eventually approaches a fixed point corresponding to the stable steady fall. In diagram (b) the trajectory departs spiraling from the unstable fixed point and converges to a limit cycle of the second kind around the cylinder, which corresponds to the autorotation. Figure 7 illustrates the respective spatial motions of the plate in the fluid.

Despite the simplicity of the Kozlov model, it manifests nontrivial phenomena of nonlinear dynamics, such as transition to chaos through period doubling, strange attractors, and multistability in certain parameter regions (see Section 8.2).

[1)] Strictly speaking, this limit produces a nonuniform mass distribution on the plate with density decreasing from central maximum to the edges as $\sqrt{a^2-x^2}$. Unlike the moment of inertia $\frac13ma^2$ of a homogeneous plate, in this limit we have $\frac14ma^2$. However, in the framework of qualitative analysis, this difference seems insignificant.

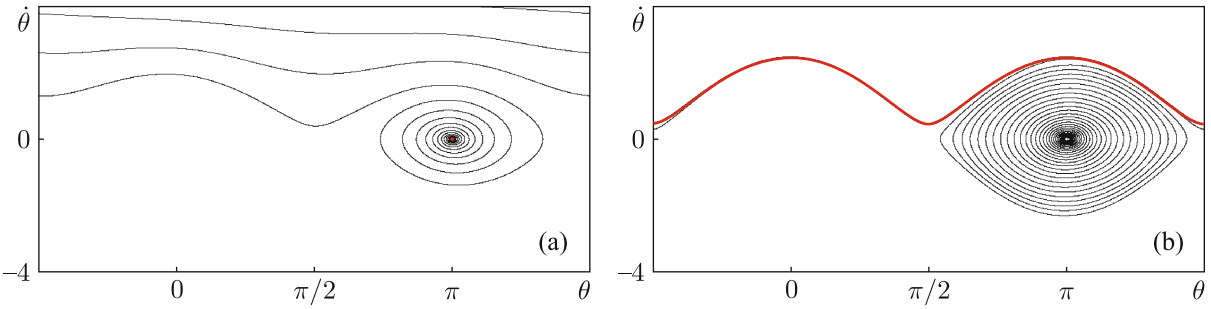

Fig. 6. Phase trajectories in the Kozlov model (3.16) with $r = 2$, $k_2 = 1$, $k_3 = 0.04$, $k_1 = \frac{1}{3}$ (a), and $k_1 = \frac{1}{5}$ (b). The attractors are shown in red; this is a fixed point in panel (a) and a limit cycle of the second kind responsible for autorotation in panel (b).

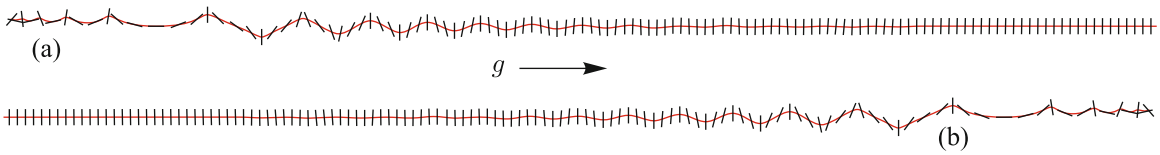

Fig. 7. The spatial motion of the falling plate in the Kozlov model with parameters corresponding to panels (a) and (b) in the previous figure.

To conclude this Section, we mention briefly the work of Mahadevan [26], where the problem formulation is similar to that of Kozlov, but the nonlinear dependence of the drag force on the velocity is taken into account. The author defines the nonlinear friction in such a way that the drag coefficient for each component of the force depends only on the velocity component in the same direction, which is hardly justified.The model takes into account a possible displacement of the center of mass of the body relative to the geometric center of the elliptic profile and the possibility of nonzero circulation around the profile, which is considered as a constant parameter Γ. Analytical results are consistent with those of Kozlov, with the addition that the asymmetric case is considered. Numerical results are scarce. They are irreproducible because of obvious errors specifying relevant parameters in the text of the article.

4. LORENZ ATTRACTOR IN THE MODEL OF BODY MOTION IN A FLUID

The Lorenz attractor [46–48] is a popular object of nonlinear dynamics and has been well studied by mathematicians. It relates to the class of quasi-hyperbolic (or singular hyperbolic) strange attractors. Chaotic dynamics on the Lorenz attractor are rigorously stated and justified [49].

Here we demonstrate that the motion of a body of elliptical profile in a viscous fluid may be associated with the Lorenz-type attractor.

Under assumptions of the Kozlov model (3.6), consider a case of equal densities $\rho = 1$, when the effect of gravity is excluded (i. e., $P = 0$), and assume the presence of constant nonzero circulation Γ. Additionally, in the equation for the angular velocity we include a term of a constant external torque M. So, we arrive at the equations

$$\begin{aligned} A\dot u &= Bvw - \Gamma v - \mu_1 u,\\ B\dot v &= -Auw + \Gamma u - \mu_2 v,\\ Q\dot w &= -(B-A)uv - \mu_3 w + M, \end{aligned} \tag{4.1}$$

where $w = \dot\theta$. By the change of variables and parameters

$$u = x\sqrt{A^{-1}BQ/(B-A)}, \quad v = y\sqrt{AB^{-1}Q/(B-A)}, \quad w = M\mu_3^{-1} - z, \tag{4.2}$$

$$\begin{aligned} \nu_1 &= \mu_1 A^{-1}, \quad h_1 = M\mu_3^{-1} - \Gamma B^{-1},\\ \nu_2 &= \mu_2 B^{-1}, \quad h_2 = \Gamma A^{-1} - M\mu_3^{-1},\\ \nu_3 &= \mu_3 Q^{-1}, \end{aligned} \tag{4.3}$$

the equations are reduced to the form similar to the Lorenz model:

$$\begin{aligned} \dot{x} &= h_1 y - \nu_1 x - yz, \\ \dot{y} &= h_2 x - \nu_2 y + xz, \\ \dot{z} &= -\nu_3 z + xy. \end{aligned} \tag{4.4}$$

In the case $h_1 = h_2$ they coincide exactly with equations for parametric excitation of waves considered by Pikovsky, Rabinovich and Trahtengerts [50] who demonstrated the Lorenz-type attractor, e. g., at $\nu_1 = 1$, $\nu_2 = 4$, $\nu_3 = 1$, $h = 5.875$. With these values, taking arbitrarily $\beta = 0.25$ and, respectively, $A = 1 + \beta = 1.25$, $B = 1 + \beta^{-1} = 5$, $Q = \frac{1}{4}(1 + \beta^2) + \frac{1}{8}\beta^{-1}(1 - \beta^2)^2 = 0.705$, we obtain from (4.3)

$$\mu_1 = 1.25, \quad \mu_2 = 20, \quad \mu_3 = 0.705, \quad M = 6.903, \quad \Gamma = 19.583. \tag{4.5}$$

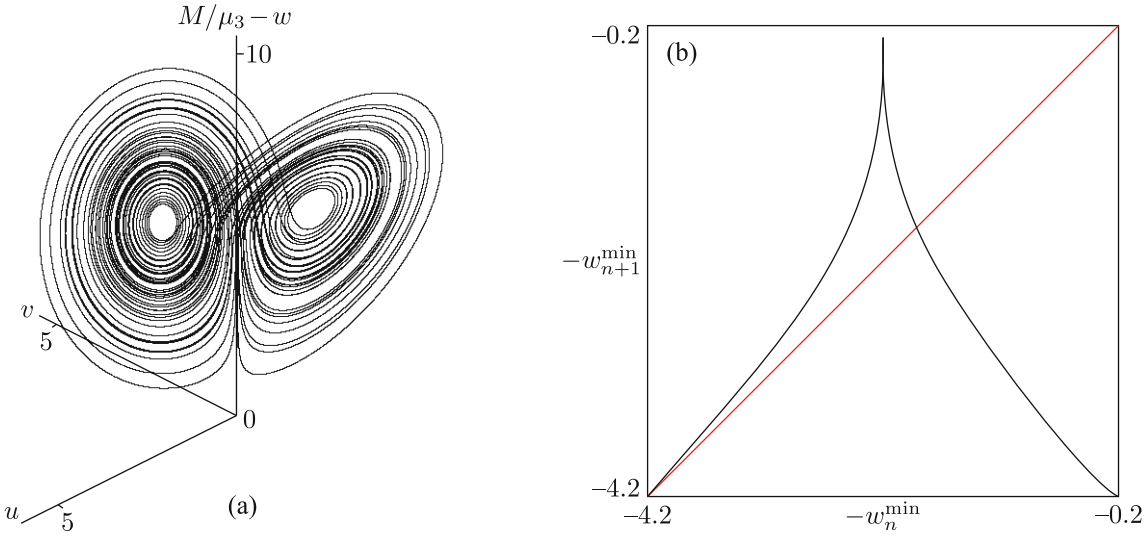

Fig. 8. Lorenz-type attractor in three-dimensional state space (a) and plot of the map for consecutive minima of the variable w in the course of time evolution (b). The diagrams are based on the data of numerical solution of equations (4.1) with $\mu_1 = 1.25$, $\mu_2 = 20$, $\mu_3 = 0.705$, $M = 6.903$, $\Gamma = 19.583$.

Figure 8 shows a three-dimensional portrait of the attractor in the phase space of the system (4.1) obtained from numerical solution of the equations with these parameters and a diagram for the map prepared according to the procedure proposed in the original paper of Lorenz [46], where successive minima of the variable w achieved during the time evolution of the system are plotted. Observe the characteristic form with a sharp maximum, which resembles a classic "saw tooth" map [14, 15, 46, 47, 50] that supports the quasi-hyperbolic nature of the attractor similar to the classic Lorenz attractor.

Figure 9 provides portraits of the attractor in the planes of the variables u, v and $\varphi = \arg(u + iv)$, $w = \dot{\theta}$, which can be compared with the diagrams for other models discussed in this review. From diagram (b) it is clear that the dynamics must be interpreted as chaotic rotation.

Figure 10 illustrates the real space-time motion of the body associated with dynamics on the Lorenz attractor in the subspace of the generalized velocities. To draw this diagram, the numerical solution of Eqs. (4.1) is carried out together with the equations for the angular velocity and for the coordinates of the center of mass

$$\dot{\theta} = w, \quad \dot{X} = u\cos\theta - v\sin\theta, \quad \dot{Y} = u\sin\theta + v\cos\theta. \tag{4.6}$$

The figure shows that the motion is accompanied by chaotic oscillations and tumbling of the body according to the chaotic nature of the attractor.

To quantify the characteristics of chaos, it is appropriate to use the Lyapunov exponents. The full spectrum of Lyapunov exponents of the system (4.1), (4.6) has three zero members corresponding

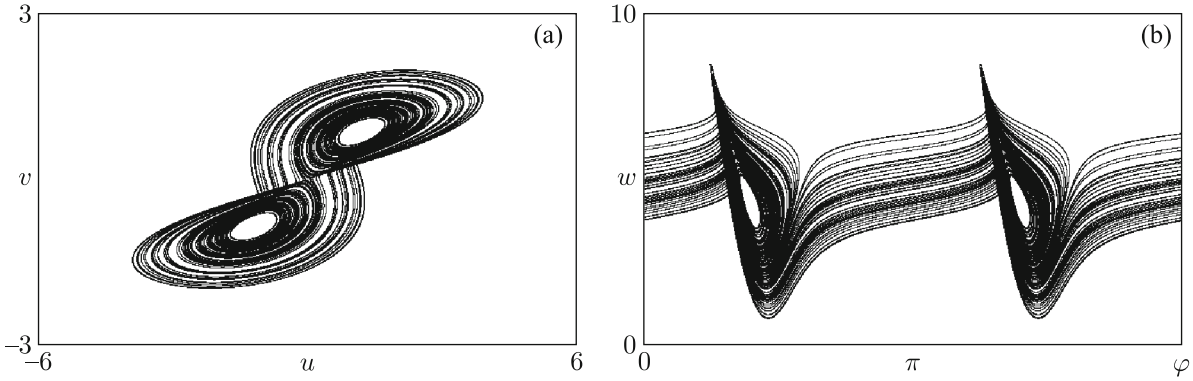

Fig. 9. Attractor of the system (4.1) as projected onto the planes of the variables (u, v) and (φ, w). The parameters are the same as those in Fig. 8. The fact that the trajectories cross the boundaries of the rectangle in diagram (b), i. e., go around the phase cylinder, indicates the rotational (tumbling) motion of the body.

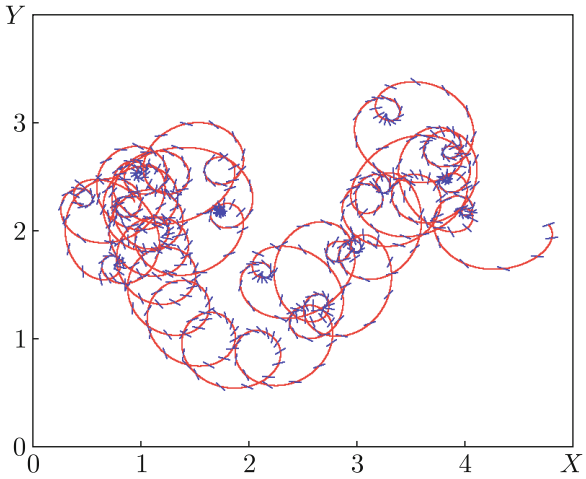

Fig. 10. Spatial motion of the body in a situation where the Lorenz attractor exists in the space of generalized velocities (u, v, w). The parameters are the same as those in Fig. 8.

to perturbations of shift of the center of mass along two coordinate axes, and to variation of the inclination angle. In addition to them, there are three nontrivial exponents relating to the Lorenz attractor of the subsystem (4.1). Their computation from simultaneous numerical solution of Eqs. (4.1) and the corresponding variation equations with the Benettin algorithm [15, 18] yields

$$\lambda_1 = 0.390 \pm 0.003, \quad \lambda_2 = -0.0002 \pm 0.0007, \quad \lambda_3 = -6.390 \pm 0.003. \tag{4.7}$$

The presence of the positive exponent in this list (4.6) indicates the occurrence of chaos, characterized by exponential sensitivity to initial conditions intrinsic to orbits on the attractor. The second exponent is zero (up to a calculation error) being associated with a perturbation of shift along the trajectory. The third exponent is negative, and it is responsible for the approach of the trajectories to the attractor. The fact that the sum of all the exponents is negative indicates the phase volume compression in the subspace (u, v, w). It is consistent with the analytical calculation of the divergence for the vector field determined by the right-hand sides of (4.1); namely, $\operatorname{div} \mathbf{F} = \partial_u f_u + \partial_v f_v + \partial_w f_w = -\mu_1/A - \mu_2/B - \mu_3/Q$ (at the assumed parameters it equals -6).

5. TANABE – KANEKO MODEL

For a correct description of the plane problem of body motion in a viscous fluid it is essential to take into account the dependence of the velocity circulation around the profile on the dynamical variables and parameters. For the body in the form of a thin flat plate the circulation can be

evaluated using the Kutta – Joukovsky – Chaplygin postulate of absence of singularity of the velocity field at the trailing edge of the profile moving in a fluid [7–12]. Then it becomes possible to evaluate the lift force using the Joukovsky theorem. Tanabe and Kaneko argue in their paper [23] that these effects may give rise to complex dynamics and chaos in the motion of the body falling in a fluid due to gravity.

Using the velocity components in the coordinate system attached to the body, one can simplify the equations suggested originally by Tanabe and Kaneko [23] and represent them as

$$\begin{aligned} &\dot v_x + k_\parallel v_x = \dot\theta v_y - g_0 \sin\theta + \pi\overline{\rho} v_y^2 \operatorname{sgn} v_x, \\ &\dot v_y + k_\perp v_y = -\dot\theta v_x - g_0 \cos\theta - \pi\overline{\rho} v_x v_y \operatorname{sgn} v_x, \\ &\ddot\theta + k_\perp \dot\theta = -3\pi\overline{\rho} l^{-1} v_x v_y, \end{aligned} \tag{5.1}$$

where $\overline{\rho} = \rho_f l/m$, $l = 2a$ is the width of the plate, g_0 is the gravity acceleration constant, and m is the mass of the plate. The coefficients $k_\parallel$ and $k_\perp$ characterize the viscous friction for the motion of the plate in a fluid in the longitudinal and the transverse direction. To determine the coordinates of the center of mass in the laboratory frame, the system (5.1) is supplemented by the equations

$$\dot X = v_x \cos\theta - v_y \sin\theta, \quad \dot Y = v_x \sin\theta + v_y \cos\theta. \tag{5.2}$$

In the absence of friction, Eqs. (5.1) obviously correspond in structure to Eqs. (1.6) if we set

$$\Gamma = -\pi l v_y \operatorname{sgn} v_x, \quad A = B = 1, \quad \frac{A-B}{a^2 Q} = -\frac{3\pi\overline{\rho}}{l}, \quad g(1-\rho) = g_0. \tag{5.3}$$

The fact that the second and the third equalities of (5.3) contradict each other is due to some incorrectness of the Tanabe – Kaneko formulation of the problem, which was criticized after publication of their work [24, 25]. Namely, since the authors excluded the added mass effect, the coefficients A and B appear to be equal, and this implies that the coefficient in the third equation of (5.1) vanishes, while in a correct approach it should be relevant for the observed complex dynamics. Further, the formula for circulation Γ according to (5.3) takes into account only contribution of the translational motion of the plate, while there is also a contribution from the rotational motion proportional to the angular velocity [9, 28]. In addition, Tanabe and Kaneko excluded the Archimedean buoyancy.[2)]

Despite these seemingly essential deficiencies, the Tanabe – Kaneko model qualitatively gives a reasonable picture of possible regimes of complex dynamics for a plate falling in a fluid. This is confirmed by comparative analysis of this model with its corrected version and explained to some extent in Section 8.3.

We present here some numerical results for the model (5.1), taking the parameters chosen by the authors: $\overline{\rho} = 0.1$, $l = 1$, $g_0 = 9.8$; the values $k_\parallel$ and $k_\perp$ will be varied.

To define the Poincaré map, it is appropriate to determine the cross-section of the flow of trajectories in four-dimensional phase space by a three-dimensional hypersurface

$$S = \sin\theta = 0. \tag{5.4}$$

Calculation of the Poincaré map was implemented as a special subroutine that performs numerical integration of the differential equations by the Runge – Kutta fourth-order method. To construct the Poincaré section in accordance with the condition (5.4), the method of Hénon was used [15, 51]. Specifically, numerical integration of the differential equations is continued up to detecting a situation where at the next step the value of S changes sign. Then the last step is canceled, and an additional step is performed using the same difference method, but taking S as the independent variable, and with the step size given by the obtained value of S with the opposite sign. This returns the representative point to the surface $S = 0$ and we get the Poincaré map image for the initial state vector. Note that the procedure is consistent in accuracy with the difference scheme used. A similar routine is performed at intersections of the phase trajectory with

[2)] The last flaw, however, may be corrected readily by introducing a parameter of effective acceleration of free fall, $g_0 = g(1-\rho)$, and in some cases, like the fall of the plate in the air, it is naturally insignificant.

the three-dimensional hypersurface $u = 0$ to avoid loss of accuracy of the difference scheme by accurate localization of the passages in time.

To draw charts of dynamical regimes, a procedure of scanning the parameter plane of $k_\perp$ and $f = k_\perp/k_\parallel$ is carried out on a grid with some steps along two coordinate axes. At each point about 10^3 iterations of the Poincaré map are produced, and the data for the final iteration steps are analyzed to detect a repetition period (from 1 to 14) up to some level of permissible error. If a certain period is detected, the pixel in the diagram is attributed with the corresponding color, and the routine proceeds with analysis of the next point in the parameter plane. To start iterations at each new point, it is reasonable to use a state obtained as a result of iterations at the previous point ("scan with inheritance"). In most cases it helps to speed up essentially the convergence to sustained dynamics.

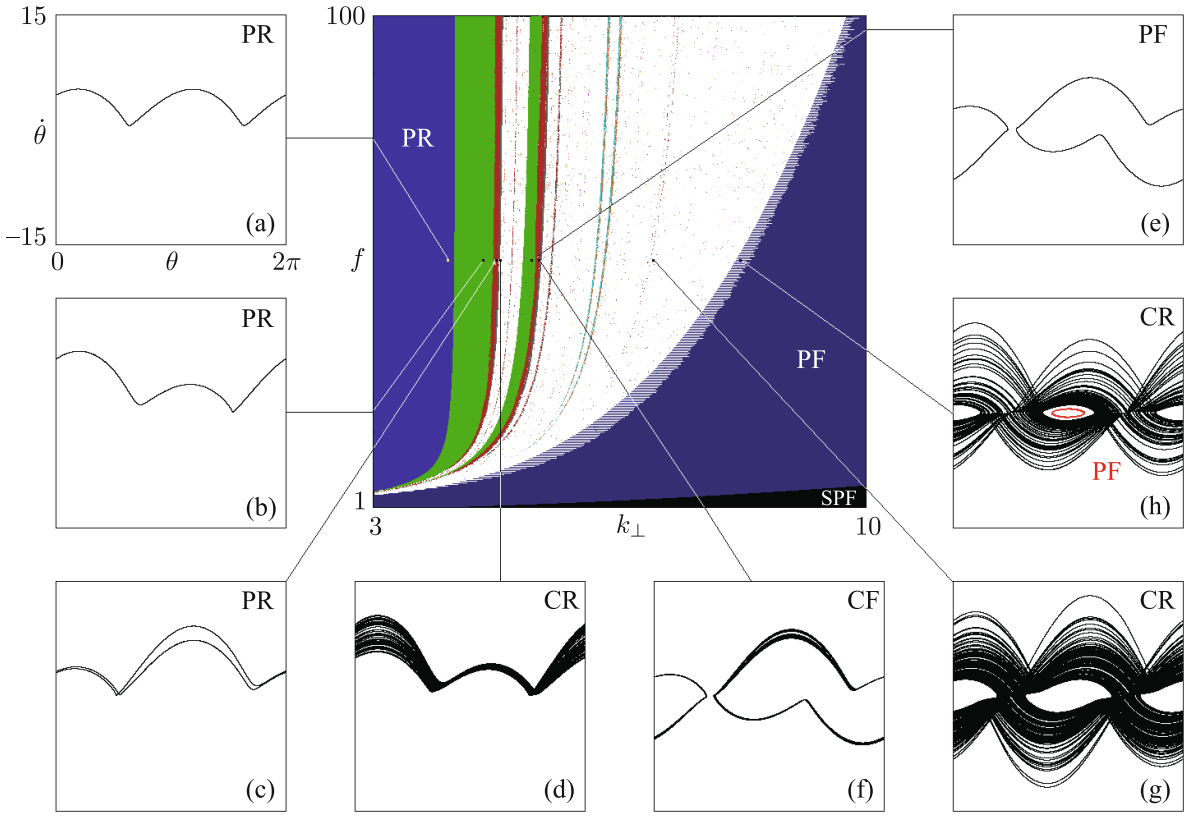

Fig. 11. Chart of dynamical regimes in the parameter plane $k_\perp$, $f = k_\perp/k_\parallel$ for the Tanabe – Kaneko model. The values of the other parameters are $\overline{\rho} = 0.1$, $l = 1$, $g = 9.8$. The color is determined from analysis of the repetition period in the Poincaré section (blue denotes period-1 with symmetry, and green without symmetry, the other colors correspond to larger periods). White denotes chaos or unrecognized regular regimes. Black indicates stationary fall (SPF). On the periphery the portraits of attractors are shown for regimes corresponding to the Tanabe – Kaneko classification scheme: PR (periodic rotation), CR (chaotic rotation), RF (periodic flutter, oscillations without tumbling), CF (chaotic flutter). Blue and white horizontal shading corresponds to coexistence of attractors associated with chaotic rotation and periodic oscillations, as illustrated in diagram (h).

Figure 11 shows a chart of dynamical regimes. On the periphery the portraits of attractors are collected corresponding to some representative points on the parameter plane. Visually, the phase portraits in the plane $(\theta, \dot\theta)$ directly indicate a nature of the regimes of the fall. If the orbit or a set of orbits belonging to the attractor goes around the phase cylinder, the regime is classified as autorotation that may be periodic (PR, diagrams (a), (b), (c)) or chaotic (CR, diagrams (d), (g), (h)). If no orbits around the phase cylinder occur, this corresponds to a fall with oscillations without tumbling that is flutter, which may be periodic (PF, diagram (e)), or chaotic (CF, diagram (f)).

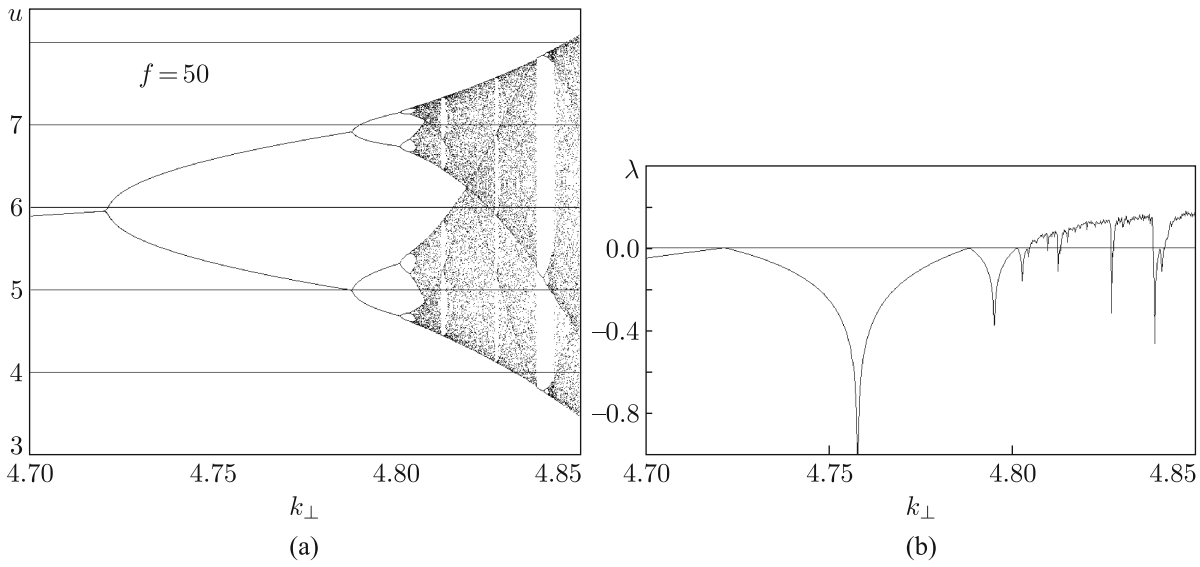

Fig. 12. Bifurcation tree and the parameter dependence of the largest nontrivial Lyapunov exponent illustrating the transition to chaos through period doubling bifurcations in the Tanabe – Kaneko model along the horizontal path $f = 50$ on the chart of regimes of Fig. 11.

The black area at the bottom left of the chart corresponds to the steady perpendicular fall without oscillations (SPF).

The full spectrum of Lyapunov exponents of the system (5.1), (5.2) includes two zero exponents corresponding to shift perturbations for coordinates X and Y of the center of mass, and four exponents relating to the attractor of the subsystem (5.1). One of them is zero; it is associated with a shift along the reference phase trajectory on the attractor.

Because of the presence of a discontinuous sgn-function in (5.1), it is preferable to compute Lyapunov exponents without appealing to the linearized equations in variations [15]. Namely, at given parameters, using the subroutine for computing the Poincaré map, we perform iterations jointly for a collection of four states, one of which corresponds to the reference trajectory, and the three others correspond to slightly perturbed orbits close to the reference one. After each step, the perturbation vectors are orthogonalized by the Gram – Schmidt procedure and normalized to a fixed small norm, and the computation continues with the redefined perturbation vectors. Three nontrivial Lyapunov exponents are evaluated as coefficients of the growth or decay of the accumulated sums of the logarithm of the perturbation magnitude ratios.

As is well known, in systems with symmetry a symmetric limit cycle cannot undergo a period doubling; the symmetry breaking bifurcation must precede (see [52]).

Increasing the value of $k_\perp$, i. e., moving on the chart of Fig. 11 along a horizontal path from left to right, one observes the symmetry breaking corresponding to transition from the blue to the green area and then it is followed by a cascade of period doubling bifurcations and the onset of chaos.

Figure 12 shows a one-parameter bifurcation diagram ("bifurcation tree") and the parameter dependence of the senior nontrivial Lyapunov exponent illustrating the period doubling transition to chaos. Diagrams correspond to the horizontal path on the chart at $f = 50$. The diagrams demonstrate a well-recognizable typical visual image of transition to chaos through an infinite cascade of period doubling bifurcations manifesting universality and scaling of Feigenbaum [14, 15, 54, 55]. This qualitative conclusion is confirmed by numerical estimates for the constants of convergence of bifurcation points ($\delta \approx 4.67$) and of splitting of the branches of the "tree" ($\alpha \approx -2.50$).

Figure 13 reproduces portraits of attractors for Tanabe – Kaneko model similar to those in their original paper. The components of translational velocity in the laboratory frame determined according to (5.2) are plotted along the coordinate axes. The Lyapunov exponents of these attractors (except zero ones, related to the subsystem (5.2)) obtained in the computations are listed in the

figure caption. The attractor in diagram (a) is regular and consists of a single closed orbit that is a limit cycle. The senior exponent here is zero, and the others are negative. The attractors (b) and (c) are characterized by the presence of a positive exponent that indicates the chaotic nature of the regime. The sum of the exponents in each case is negative, which means compression of the phase volume in the subspace $(u,\, v,\, \theta,\, \dot\theta)$ in the course of time evolution. Its value is consistent with analytical calculation of the divergence of the vector field whose components are given by the right-hand side of (5.1): $\operatorname{div}\mathbf{F} = -k_{\parallel} - 2k_{\perp}$.

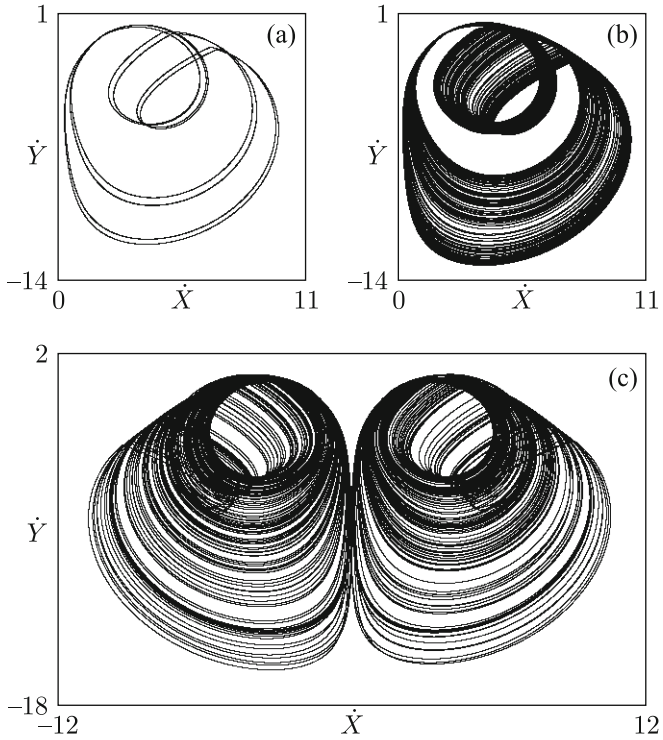

Fig. 13. Phase portraits of attractors for the Tanabe – Kaneko model at $k = 4.84$ (a), 4.9 (b), 5 (c). The other parameters are: $\overline{\rho} = 0.1,\ l = 1,\ g = 9.8,\ k_{\parallel} = 100k$. The components of translational velocity in the laboratory frame $\dot X = v_x\cos\theta - v_y\sin\theta,\ \dot Y = v_x\sin\theta + v_y\cos\theta$ are plotted along the coordinate axes. The Lyapunov exponents are: a) $\{0,\, -0.085,\, -2.026,\, -7.62\}$, b) $\{0.162 \pm 0.005,\, 0,\, -2.23 \pm 0.01,\, -7.78 \pm 0.1\}$, c) $\{0.345 \pm 0.007,\, 0,\, -2.36 \pm 0.01,\, -7.86 \pm 0.05\}$.

Let us discuss in some detail the transition from a steady fall to oscillations (flutter) in the Tanabe – Kaneko model. A nonstandard nature of the bifurcation occurs due to the fact that the equations contain a discontinuous function sgn.

To consider solutions close to the steady fall regime: $\theta = 0,\ v_x = 0,\ v_y = -g_0/k_{\perp}$, we put $\theta = \vartheta,\ v_x = u,\ v_y = -g_0k_{\perp}^{-1} + v$, where $|\vartheta| \ll 1,\ |u| \ll 1,\ |v| \ll 1$. If we ignore perturbations of the transverse velocity v_y (with relatively large factor $k_{\perp}$ it seems reasonable), the equations for the other variables read

$$\begin{aligned} &\dot u + k_{\parallel}u + g_0\xi = \pi\overline{\rho}g_0^2k_{\perp}^{-2}\operatorname{sgn}u,\\ &\dot\xi = 3\pi\overline{\rho}g_0l^{-1}k_{\perp}^{-2}u, \end{aligned} \tag{5.5}$$

where $\xi = k_{\perp}^{-1}\dot\vartheta + \vartheta$. Hence, for ξ we obtain an equation of the same form as that for an oscillator with dry friction [53]

$$\ddot\xi + k_{\parallel}\dot\xi + \omega^2\xi = F\operatorname{sgn}\dot\xi, \tag{5.6}$$

with $\omega^2 = 3\pi\overline{\rho}g_0^2 l^{-1}k_\perp^{-2}$, $F = 3\pi^2\overline{\rho}^2 g_0^3 l^{-1}k_\perp^{-4}$. However, the factor responsible for the "dry friction" has a sign opposite to that in the standard problem.

First, let us assume for simplicity that $k_\parallel = 0$. In the upper half-plane $(\xi, \dot\xi)$ the family of phase trajectories is represented by ellipses centered on the x-axis at $\xi = F\omega^{-2} = \pi\overline{\rho}gk_\perp^{-2}$ (point A in Fig. 14a), and in the lower half-plane by ellipses centered at $\xi = -F\omega^{-2}$ (point B in Fig. 14a). Since $F > 0$, the resulting motion is accompanied by the growing oscillations (the amplitude increases linearly in time).

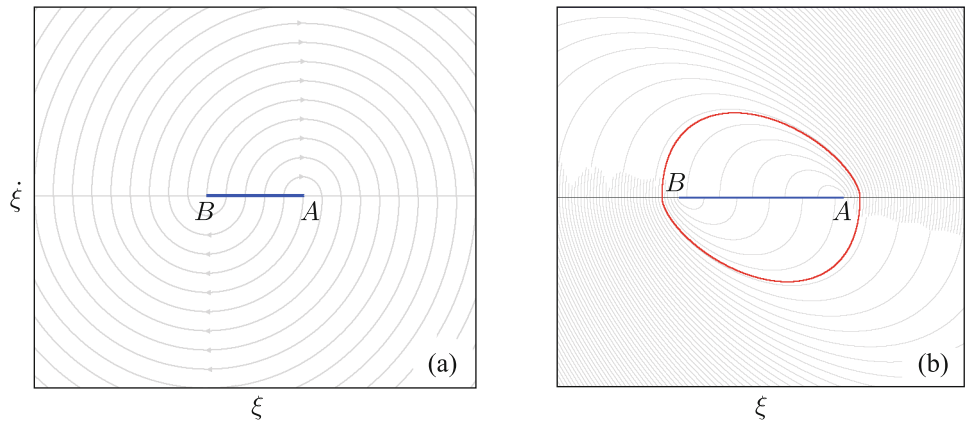

Fig. 14. Phase trajectories for Eqs. (5.6) on the plane $(\xi, \dot\xi)$ in the case $k_\parallel = 0$ (a) and for $0 < k_\parallel < k_*$ (b). The horizontal segment AB consists of unstable fixed points. The stable limit cycle is shown in red in diagram (b).

Suppose now that the coefficient $k_\parallel$ is positive. While it is not large, in the upper half-plane instead of ellipses we have a family of trajectories spiraling to point A, and in the lower half-plane to the point B. The corresponding oscillation frequency and the damping coefficient are determined by the imaginary and real parts of the roots of the characteristic equation $\lambda^2 + k_\parallel\lambda + \omega^2 = 0$: $\lambda_{1,2} = k_\parallel/2 \pm i\sqrt{\omega^2 - k_\parallel^2/4}$. In contrast to the previous case, the oscillating motion of the representative point visiting alternately the upper and lower half-planes converges to a limit cycle encompassing the segment AB. The situation will change when the character of the decay becomes not oscillating but monotonous, which corresponds to the case $k_\parallel^2 > 4\omega^2$. Returning to the parameters of the Tanabe – Kaneko model, we see that this corresponds to the condition

$$f = \frac{k_\perp}{k_\parallel} < \left(\frac{k_\perp}{k_*}\right)^2, \quad k_* = \sqrt[4]{12\frac{\pi\overline{\rho}g_0^2}{l}}. \tag{5.7}$$

In the chart of regimes the corresponding area is shown in black. Numerical simulations show that in this area the steady fall occurs, while outside it the oscillations (flutter) develop.[3)]

6. BELMONTE – EISENBERG – MOSES MODEL

Starting from some experiments with plates falling in a fluid, the authors [27] turn to a formulation of the problem in which the resistance forces for the translational and rotational motions depend on the velocities quadratically:

$$F_x = -\frac{1}{4}\alpha_\parallel\rho_f lV v_x, \quad F_y = -\frac{1}{4}\alpha_\perp\rho_f lV v_y, \quad F_\theta = -\frac{1}{4}\alpha_\omega\rho_f l^4|\dot\theta|\dot\theta, \tag{6.1}$$

[3)] The simplified equation (5.1) can be considered as a reasonable approximation until $\vartheta < 1$. Since $|\vartheta| \sim |\xi_{A,B}|$, this implies $|\xi_{A,B}| < 1$. With $\overline{\rho} = 0.1$, $l = 1$ and $g = 9.8$ we have $k_* = 4.36$ and $\pm\xi_{A,B} = \pi\overline{\rho}gk_\perp^{-2} \approx 3k_\perp^{-2}$, so the inequality $3k_\perp^{-2} < 1$ is a condition for validity of (5.1). The black area in the chart of regimes is located in a part of the parameter plane where this condition is well satisfied.

where $V = \sqrt{v_x^2 + v_y^2}$, $\alpha_\parallel$, $\alpha_\perp$, and α_ω are constant coefficients. Equations analogous to those of Tanabe – Kaneko in this case take the form

$$\begin{aligned}
\dot v_x &= -\frac{1}{4}\alpha_\parallel \overline{\rho} V v_x - g^* \sin\theta + \pi\overline{\rho} v_y^2 \operatorname{sgn} v_x + \dot\theta v_y, \quad V = \sqrt{v_x^2 + v_y^2},\\
\dot v_y &= -\frac{1}{4}\alpha_\perp \overline{\rho} V v_y - g^* \cos\theta - \pi\overline{\rho} v_x v_y \operatorname{sgn} v_x - \dot\theta v_x,\\
\ddot\theta &= -3\alpha_\omega \overline{\rho} l |\dot\theta| \dot\theta + 3 l^{-1} \pi \overline{\rho} v_x v_y,
\end{aligned} \tag{6.2}$$

where the same notation is used as in (5.1), and the constant g^* characterizes the acceleration of gravity reduced with the Archimedean buoyancy taken into account.

The authors emphasize the fact that due to the quadratic dependence of the resistance forces the above equations rewritten in a dimensionless form contain a characteristic parameter well known in hydrodynamics, the Froude number Fr. Namely, the change of variables and parameters

$$v_x = 2v_x'\sqrt{\frac{g^*}{\overline{\rho}}}, \quad v_y = 2v_y'\sqrt{\frac{g^*}{\overline{\rho}}}, \quad t = t'\sqrt{\frac{l}{g^*}}, \quad \mathrm{Fr} = \frac{2}{\sqrt{\overline{\rho} l}} \tag{6.3}$$

reduces Eqs. (6.2) to

$$\begin{aligned}
\dot v_x &= (-\alpha_\parallel V v_x - \sin\theta + 4\pi v_y^2 \operatorname{sgn} v_x)/\mathrm{Fr} + \dot\theta v_y, \quad V = \sqrt{v_x^2 + v_y^2},\\
\dot v_y &= (-\alpha_\perp V v_y - \cos\theta - 4\pi v_x v_y \operatorname{sgn} v_x)/\mathrm{Fr} - \dot\theta v_x,\\
\ddot\theta &= -12 \cdot \alpha_\omega |\dot\theta| \dot\theta/\mathrm{Fr}^2 + 12\pi v_x v_y,
\end{aligned} \tag{6.4}$$

where the primes are omitted for brevity. The authors take the values of the coefficients

$$\alpha_\parallel = 0.88, \quad \alpha_\perp = 4.1, \quad \alpha_\omega = 0.0674. \tag{6.5}$$

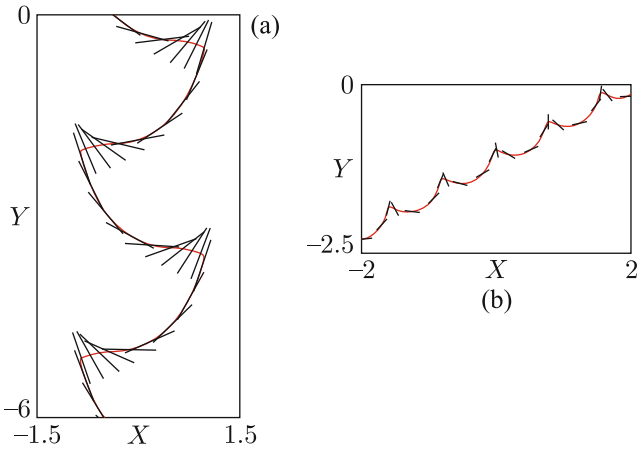

Fig. 15. Illustrations of motion of a plate in a fluid: self-oscillation mode at Fr = 0.45 (a) and autorotation at Fr = 0.89 (b) according to results of numerical simulation with Eqs. (6.4).

Figure 15 shows the diagrams obtained by numerical integration of (6.4), which reproduce the results of [27]. Illustrations (a) and (b) correspond to the fall with oscillations (flutter) and tumbling (autorotation), respectively. Figure 16 shows portraits of attractors corresponding to these motions as projected onto the planes (v_x, v_y) and $(\theta, \dot\theta)$. From the diagrams in the right column one can see that in one case the observed motion corresponds to the limit cycle of the first kind, and in the other case it corresponds to the limit cycle of the second kind (going around the phase cylinder).

Like the original Tanabe – Kaneko model, the model (6.2) takes into account neither the added masses nor the moment of inertia nor a correction to the circulation due to the rotational motion. So it makes sense to consider a modification of the equations in the same style as in the corrected Tanabe – Kaneko model (see Section 8).

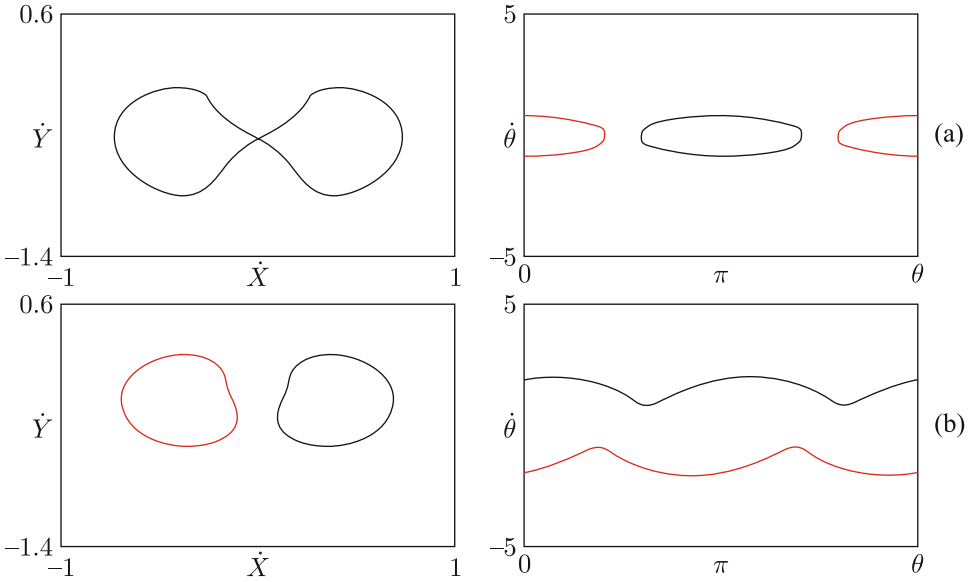

Fig. 16. Phase portraits of attractors corresponding to flutter at Fr = 0.45 (a) and to autorotation at Fr = 0.89 (b) according to the results of the numerical solution of Eqs. (6.1). The coexisting attractors are shown in black and red.

7. ANDERSEN – PESAVENTO – WANG MODEL

Among the systems discussed in this review, the work of Andersen, Pesavento and Wang [28] is the most elaborated attempt to describe the fall of a flat plate or a body with elliptic profile in a fluid by means of a finite-dimensional model. The authors start with Eqs. (1.2) and add to them terms responsible for the resistance of the medium to the translational motion, F_x, F_y, and the torque of the friction force F_θ:

$$\begin{aligned}
(m+m_x)\dot{v}_x &= (m+m_y)v_y\dot{\theta} - \rho_f\Gamma v_y - mg(1-\rho_f\rho_s^{-1})\sin\theta - F_x,\\
(m+m_y)\dot{v}_y &= -(m+m_x)u\dot{\theta} + \rho_f\Gamma v_x - mg(1-\rho_f\rho_s^{-1})\cos\theta - F_y,\\
(I+J)\ddot{\theta} &= (m_x-m_y)v_xv_y - F_\theta.
\end{aligned} \tag{7.1}$$

Based on numerical simulations with Navier – Stokes equations for the two-dimensional hydrodynamic flow around elliptic profiles [28, 30], the authors propose the following approximate expressions for the circulation and the resistance forces:

$$\begin{gathered}
\Gamma = -2C_Ta\frac{v_xv_y}{\sqrt{v_x^2+v_y^2}} + 2C_Ra^2\dot{\theta},\\
\begin{pmatrix}F_x\\F_y\end{pmatrix} = \rho_fa\left(C_A - C_B\frac{u^2-v^2}{v_x^2+v_y^2}\right)\sqrt{v_x^2+v_y^2}\begin{pmatrix}v_x\\v_y\end{pmatrix},\\
F_\theta = \pi\rho_fa^4\left(\mu_1+\mu_2|\dot{\theta}|\right).
\end{gathered} \tag{7.2}$$

In calculations, the following numerical values of the coefficients are assumed:

$$C_T = \frac{6}{5}, \quad C_R = \pi, \quad C_A = \frac{7}{5}, \quad C_B = 1, \tag{7.3}$$

while μ_1 and μ_2 are supposed to be varied.

Let us substitute the expressions (1.4) and (1.5) for the mass, the moment of inertia, the added masses, and the added moment of inertia in Eq. (7.1) and introduce the notation

$$I^* = \frac{b\rho_s}{a\rho_f}, \quad \beta = \frac{b}{a}. \tag{7.4}$$

Rescaling the velocity components and time to get the unit coefficients in the terms responsible for gravity,

$$u = \frac{v_x}{a\sqrt{gI^*(1-\rho)}}, \quad v = \frac{v_y}{a\sqrt{gI^*(1-\rho)}}, \quad t' = t\sqrt{gI^*(1-\rho)}, \tag{7.5}$$

we obtain

$$\begin{aligned} &(I^* + \beta^2)\dot{u} = (I^* + 1)v\dot{\theta} - \overline{\Gamma}v - \sin\theta - Ku, \\ &(I^* + 1)\dot{v} = -(I^* + \beta^2)u\dot{\theta} + \overline{\Gamma}u - \cos\theta - Kv, \\ &\left(\frac{1}{4}(1+\beta^2)I^* + \frac{1}{8}(1-\beta^2)^2\right)\ddot{\theta} = (\beta^2 - 1)uv - K_\theta\dot{\theta}. \end{aligned} \tag{7.6}$$

In the limit $\beta \to 0$ corresponding to the thin flat plate, the equations reduce to

$$\begin{aligned} &I^*\dot{u} = (I^* + 1)v\dot{\theta} - \overline{\Gamma}v - \sin\theta - Ku, \\ &(I^* + 1)\dot{v} = -I^*u\dot{\theta} + \overline{\Gamma}u - \cos\theta - Kv, \\ &\left(\frac{1}{4}I^* + \frac{1}{8}\right)\ddot{\theta} = -uv - K_\theta\dot{\theta}. \end{aligned} \tag{7.7}$$

In accordance with (7.2), in (7.6) and (7.7) we set

$$\begin{gathered} \overline{\Gamma} = \frac{2}{\pi}\left(-C_T\frac{uv}{\sqrt{u^2+v^2}} + C_R\dot{\theta}\right), \quad K = \frac{1}{\pi}\left(C_A - C_B\frac{u^2-v^2}{u^2+v^2}\right)\sqrt{u^2+v^2}, \\ K_\theta = \mu_1' + \mu_2|\dot{\theta}|, \quad \mu_1' = \mu_1\sqrt{gI^*(1-\rho)}. \end{gathered} \tag{7.8}$$

To compute the dimensionless coordinates for the center of mass of the falling body, together with (7.6) or (7.7) the equations have to be solved

$$\dot{X} = u\cos\theta - v\sin\theta, \quad \dot{Y} = u\sin\theta + v\cos\theta. \tag{7.9}$$

Without emphasizing this point, Anderson, Pesavento and Wang [28] restrict their attention to a special case, introducing coefficients that satisfy, accidentally or not, the relation $C_T = \frac{1}{2}(C_A + C_B)$. Due to this, some terms in the equations disappear, and the derivation of the stability loss condition for the uniform steady fall simplifies substantially. The equations reduce to the form

$$\begin{aligned} &I^*\dot{u} = (I^* - 1)v\dot{\theta} - \frac{2u^3}{5\pi\sqrt{u^2+v^2}} - \sin\theta, \\ &(I^* + 1)\dot{v} = (2 - I^*)u\dot{\theta} - \frac{14u^2 + 12v^2}{5\pi\sqrt{u^2+v^2}}v - \cos\theta, \\ &\left(\frac{1}{4}I^* + \frac{1}{8}\right)\ddot{\theta} = -uv - \left(\mu_1' + \mu_2|\dot{\theta}|\right)\dot{\theta}, \end{aligned} \tag{7.10}$$

and their linearization near the fixed point $u = 0$, $v = -V = -\sqrt{5\pi/12}$, $\theta = 0$, $\dot{\theta} = 0$ yields

$$I^*\dot{\widetilde{u}} = -(I^* - 1)V\dot{\widetilde{\theta}} - \widetilde{\theta}, \quad \left(\frac{1}{4}I^* + \frac{1}{8}\right)\ddot{\theta} = Vu - \mu_1'\dot{\widetilde{\theta}}. \tag{7.11}$$

The exponential substitution $\widetilde{u}$, $\widetilde{\theta} \sim e^{st}$ leads to the characteristic equation

$$s^3\left(\frac{1}{4}I^* + \frac{1}{8}\right)I^* + s^2\mu_1'I^* + s(I^* - 1)V^2 + V = 0. \tag{7.12}$$

The condition for stability loss, which consists in vanishing of the real part for a pair of complex conjugate roots, can be found if we search for a solution in the form $s = i\zeta$, where ζ is real. Then

$$\zeta^3\left(\frac{1}{4}I^* + \frac{1}{8}\right)I^* = (I^* - 1)V^2\zeta, \quad \zeta^2\mu_1'I^* = V, \tag{7.13}$$

and the critical value of the coefficient of friction is evaluated as in [28]

$$\mu_* = \frac{2I^* + 1}{8V(I^* - 1)} = \frac{1}{4}\sqrt{\frac{3}{5\pi}}\frac{2I^* + 1}{I^* - 1}. \tag{7.14}$$

The loss of stability of the fixed point corresponds to a supercritical (normal) Andronov – Hopf bifurcation [19, 44, 45], which results in the appearance of the limit cycle associated with periodic self-oscillations of the plate from side to side (the flutter) in the region $\mu_1' < \mu_*$. Note that such a bifurcation occurs only if the viscous resistance to the rotation of the body is taken into account. If the resistance torque is quadratic in the angular velocity, i. e., $\mu_1 = 0$, then near the state of steady uniform fall the linear dynamics are conservative, and a correct stability analysis should take nonlinear terms into account.

Figure 17 shows a chart of regimes of the model (7.10) in the plane of parameters I^* and μ, drawn under the condition $\mu_1' = \mu_2 = \mu$, which corresponds to a two-dimensional phase diagram in the original paper of Anderson, Pesavento, and Wang [28]. The chart is obtained by the method described above for the Tanabe – Kaneko model; scanning is performed in the upward direction with inheritance. The colored areas in the chart indicate periodicity in the iterations of the Poincaré map. The method for computation of the Poincaré map is analogous to that for the Tanabe – Kaneko model, but simpler because now the equations do not contain discontinuous coefficients.

The dotted line in the chart indicates the threshold of stability loss for the fixed point (7.14). The passage across this boundary from the black to the dark blue domain is accompanied by the appearance of self-oscillations (flutter, the domain PF). The domain PR corresponds to the periodic autorotation. Blue indicates regimes where the system manifests a single-turn limit cycle with symmetry, and green without symmetry. The other colors relate to larger periods. The white areas correspond to chaos or unrecognized high-period motions.

Figure 18 shows phase portraits of attractors for the model (7.10) at several representative points of the parameter plane (see the figure caption). The portraits are drawn on the plane of dimensionless velocity components in the laboratory frame to enable a visual comparison with analogous pictures for the Tanabe – Kaneko model in Fig. 13. Coexisting attractors can be seen in diagrams (c)–(e) shown in black and red.

The Lyapunov exponents of the attractors have been computed and are given in the figure caption. (In addition to them, there are two zero exponents in each case, relating to the subsystem (7.9).) In the cases (e) and (f) chaotic attractors occur which possess a positive Lyapunov exponent. The second exponent is zero, while the others are negative. In the cases (a)–(d) the attractors are limit cycles, in which the senior exponent is zero, and the others are negative. The sum of all the exponents in each case is negative, which is indicative of compression of the phase volume as the phase trajectories approach the attractor.

8. GENERALIZED MODEL

For the above finite-dimensional models of a body falling in a fluid it would be interesting to provide a comparison of their dynamics, but it is complicated by the fact that all the authors use different rescalings of the equations. Below we reformulate the equations in such a way that they cover all these models using common dimensionless variables and parameters. We outline specially the limit case of the profile degenerating to the thin plate. For the model of Tanabe – Kaneko, which was criticized for some hydrodynamic incorrectness [24, 25], and, analogously, for the Belmonte – Eisenberg – Moses model, we will consider improved versions taking into account those critical remarks.

8.1. Equations and Rescaling

As initial form of the equations let us take that of Anderson, Pesavento and Wang (7.1), which relates to a body of elliptical profile with semiaxes a and b that falls in a fluid in the presence of circulation Γ and resistance forces characterized by coefficients $K_{x,y,\theta}$. Assuming

$$\Gamma = \pi a^2 \overline{\Gamma}, \tag{8.1}$$

$$F_x = \pi\rho_f a^3 K_x u, \quad F_y = \pi\rho_f a^3 K_y v, \quad F_\theta = \pi\rho_f a^4 K_\theta \dot{\theta}, \tag{8.2}$$

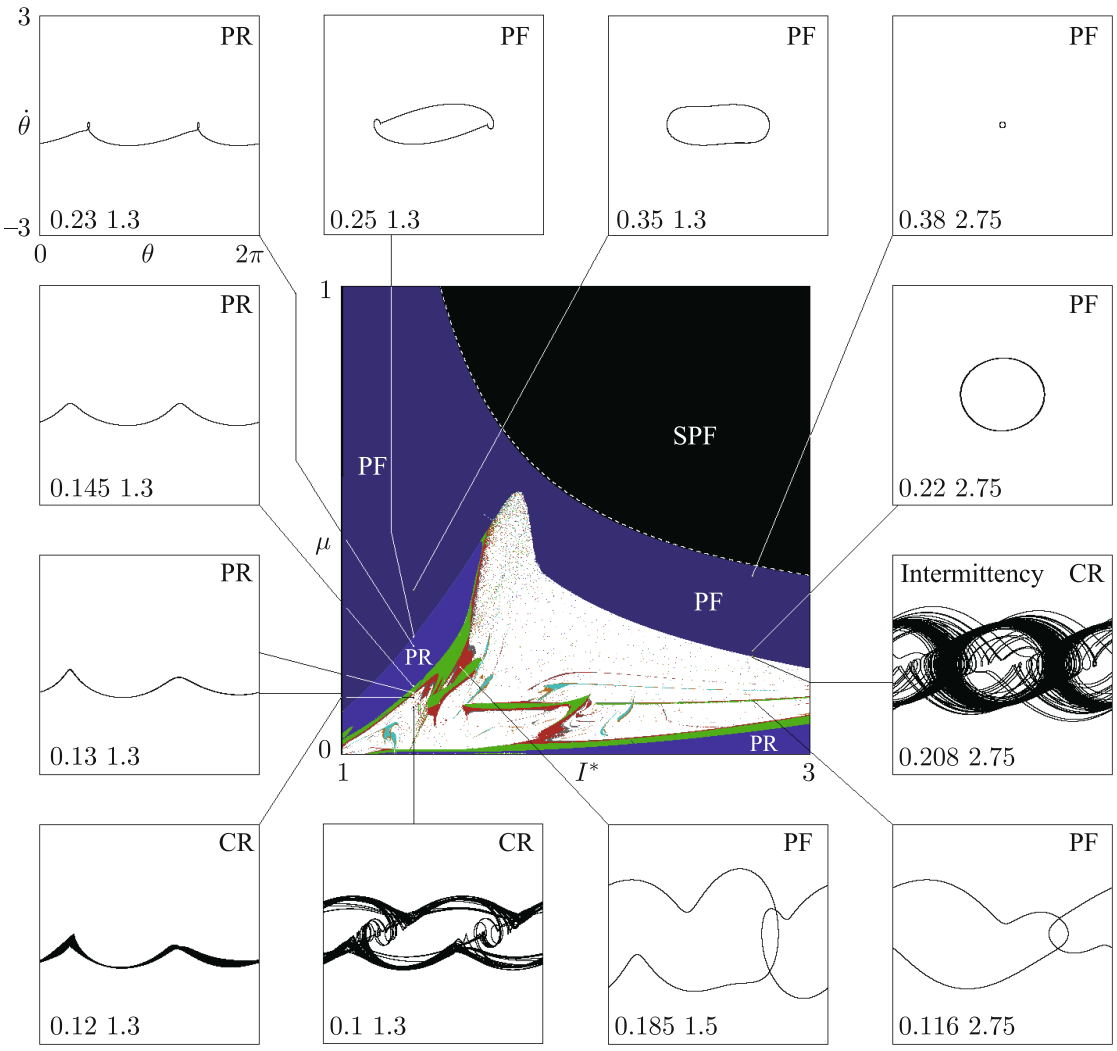

Fig. 17. Chart of regimes in the plane of parameters I^* and μ for the model (7.10), where $\mu_1 = \mu_2 = \mu$. The portraits of attractors shown on the periphery illustrate periodic rotation PR, chaotic rotation CR, periodic flutter PF, and chaotic flutter CF. The colors indicate periods observed in iterations of the Poincaré map as obtained by scanning the plane upward with inheritance. Blue indicates the period-1 regimes with symmetry, and green denotes the period-1 regimes without symmetry, the other colors correspond to larger periods. The white areas correspond to chaos or unrecognized motions. Black denotes a simple perpendicular fall (SPF). The dotted line indicates the stability loss threshold for the fixed point (7.14).

and substituting the masses and moments of inertia for the elliptical profile (1.4), (1.5) with notation $\rho = \rho_f \rho_s^{-1}$, $\beta = b/a$, $u = v_x/a$, $v = v_y/a$, we obtain from (7.1) the set of equations

$$\begin{aligned}
&(1+\rho\beta)\dot u = (1+\rho\beta^{-1})v\dot\theta - \rho\beta^{-1}\overline{\Gamma}v - ga^{-1}(1-\rho)\sin\theta - \rho\beta^{-1}K_x u,\\
&(1+\rho\beta^{-1})\dot v = -(1+\rho\beta)u\dot\theta + \rho\beta^{-1}\overline{\Gamma}u - ga^{-1}(1-\rho)\cos\theta - \rho\beta^{-1}K_y v,\\
&\left(\frac{1}{4}(1+\beta^2) + \frac{1}{8}\rho\beta^{-1}(1-\beta^2)^2\right)\ddot\theta = \rho(\beta-\beta^{-1})uv - \rho\beta^{-1}K_\theta\dot\theta.
\end{aligned} \tag{8.3}$$

In the limit corresponding to a thin plate $\beta \to 0$, $\rho \to 0$, $r = \rho\beta^{-1}$ this gives

$$\begin{aligned}
&\dot u = (1+r)v\dot\theta - r\overline{\Gamma}v - ga^{-1}\sin\theta - rK_x u,\\
&(1+r)\dot v = -u\dot\theta + r\overline{\Gamma}u - ga^{-1}\cos\theta - rK_y v,\\
&\left(\frac{1}{4}+\frac{1}{8}r\right)\ddot\theta = -ruv - rK_\theta\dot\theta.
\end{aligned} \tag{8.4}$$

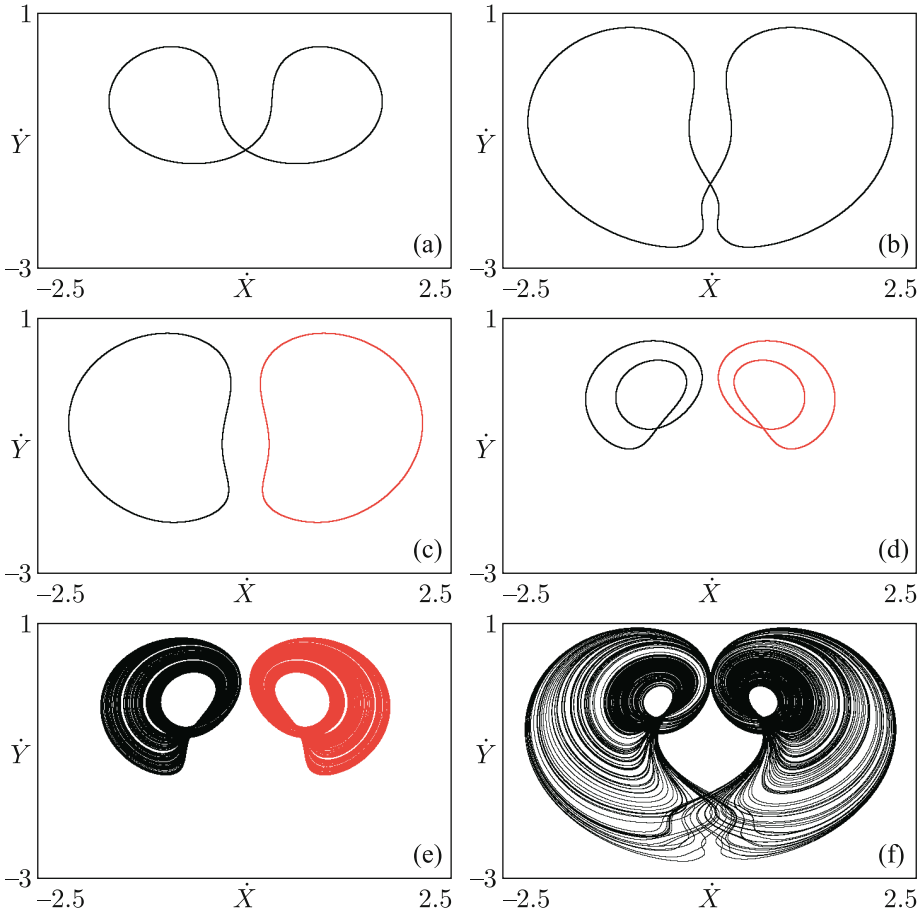

Fig. 18. Phase portraits of attractors for the Andersen – Pesavento – Wang model (7.10) at $\mu_{1,2} = 0.35$ (a), 0.25 (b), 0.23 (c), 0.13 (d), 0.12 (e), 0.1 (f). The other parameters are: $I^* = 1.3$, $C_T = 1.2$, $C_R = \pi$, $C_A = 1.4$, $C_B = 1.0$. The coexisting attractors are shown in black and red. The Lyapunov exponents for these attractors are: {0, −0.135, −0.910, −1.075} (a), {0, −0.0159, −0.871, −0.934} (b), {0, −0.158, −0.792, −0.827} (c), {0, −0.0353, −0.362, −0.766} (d), {0.051, 0, −0.435, −0.735} (e), {0.073, 0, −0.474, −0.690} (f).

As a final step, we rescale the velocity components and time as

$$u = u'\sqrt{ga^{-1}}, \quad v = v'\sqrt{ga^{-1}}, \quad t = t'\sqrt{g^{-1}a}, \tag{8.5}$$

and, omitting the primes for brevity, arrive at the equations

$$\begin{aligned} \dot{u} &= (1+r)v\dot{\theta} - r\overline{\Gamma}v - \sin\theta - rK_x u, \\ (1+r)\dot{v} &= -u\dot{\theta} + r\overline{\Gamma}u - \cos\theta - rK_y v, \\ \left(\frac{1}{4} + \frac{1}{8}r\right)\ddot{\theta} &= -ruv - rK_\theta\dot{\theta}. \end{aligned} \tag{8.6}$$

The dimensionless coordinates for the center of mass of the falling plate are determined by the equations

$$\dot{X} = u\cos\theta - v\sin\theta, \quad \dot{Y} = u\sin\theta + v\cos\theta. \tag{8.7}$$

With zero circulation $\overline{\Gamma} = 0$ and constant coefficients of the resistance forces

$$K_{x,y,\theta} = k_{1,2,3}, \tag{8.8}$$

from (8.6) we get **the Kozlov model** (3.16).

Next, let us introduce the circulation determined by the motion of the plate in a fluid on the basis of the Kutta – Joukovsky – Chaplygin postulate. It may be done using the formula from the book of

Sedov [9], which takes into account both contributions from translational and rotational components of the motion: $\Gamma = -2\pi a v_y \operatorname{sgn} v_x + \pi\dot\theta a^2$, or, using the rescaled variables and parameters,

$$\overline{\Gamma} = -2v \operatorname{sgn} u + \dot\theta. \tag{8.9}$$

Then, with the drag coefficients (8.8) we obtain from (8.6) a set of equations corresponding to **the modified Tanabe – Kaneko model**.

Postulating the same relation for the circulation (8.9) and setting

$$\begin{gathered} K_x = \alpha'_\parallel\sqrt{u^2+v^2}, \quad K_y = \alpha'_\perp\sqrt{u^2+v^2}, \quad K_\theta = \alpha'_\omega|\dot\theta|, \\ \alpha'_\parallel = \alpha_\parallel/2\pi = 0.14, \quad \alpha'_\perp = \alpha_\perp/2\pi = 0.65, \quad \alpha'_\omega = 4\alpha_\omega/\pi = 0.086, \end{gathered} \tag{8.10}$$

we arrive at **the modified Belmonte – Eisenberg – Moses model**.

Finally, using the rescaled variables and parameters, the equations of **the Anderson – Pesavento – Wang model** are obtained from (8.6) by the substitutions

$$\begin{gathered} \overline{\Gamma} = \frac{2}{\pi}\left(-C_T\frac{uv}{\sqrt{u^2+v^2}} + C_R\dot\theta\right), \quad C_T = 1.2, \quad C_R = \pi, \\ K_x = K_y = \frac{1}{\pi}\left(C_A - C_B\frac{u^2-v^2}{u^2+v^2}\right)\sqrt{u^2+v^2}, \quad C_A = 1.4, \quad C_B = 1, \\ K_\theta = \mu'_1 + \mu_2|\dot\theta|, \quad \mu'_1 = \mu_1\sqrt{g^{-1}a}. \end{gathered} \tag{8.11}$$

All the above-mentioned models have symmetries. It is useful to take them into account in analyzing the dynamical behavior.

(S1). Mirror symmetry: $u \to -u$, $v \to v$, $\theta \to -\theta$, $X \to -X$, $Y \to Y$, $\Gamma \to -\Gamma$.

(S2). Upheaval plate symmetry: $u \to -u$, $v \to -v$, $\theta \to \theta + \pi$, $X \to X$, $Y \to Y$, $\Gamma \to \Gamma$.

In the phase space of a system with symmetry, for any object, such as a regular or chaotic attractor, there are two possibilities [17]. The first is that the object itself is symmetric, i. e., it is invariant under the corresponding change of variables. The second option is that the object is asymmetric, and in this case the result of its transformation is a distinct object of the same nature, which is referred to as the symmetric partner of the original one.

8.2. Multistability and Chaos in the Kozlov Model

Although the complex dynamics in the finite-dimensional description of a falling plate was first reported by Tanabe and Kaneko, it appears in a much simpler model which does not take into account the circulation and respective forces.

As noted in Section 3, in the integrable case $k_1 = k_2/(1+r)$ the Kozlov model (3.16) reduces to the pendulum equation with damping and shows only the regular dynamics. As we depart from the condition of integrability, the loss of stability of the fixed point of the steady fall is accompanied by the Andronov – Hopf bifurcation with appearance of the limit cycle of the first kind. It is responsible for periodic self-oscillations, flutter. The limit cycle initially is located roughly inside the separatrix (in terms of the reduced model), but under variation of parameters it can approach the separatrix, passing close to saddles; this creates preconditions for emergence of complex dynamics and chaos.

Figure 19 shows a chart of regimes for the model (3.16) in the parameter plane (r, k_3) for fixed $k_1 = 0.06$ and $k_2 = 0.3$. The chart is obtained by scanning upward with inheritance. On the periphery of the chart the phase portraits of the attractors are shown as projected onto the plane of variables $(\theta, \dot\theta)$. The dotted line on the chart corresponds to the threshold of stability loss of the fixed point (3.17).

When moving in the parameter plane from the bottom upward, one observes first the bifurcation of symmetry breaking of the autorotation regime (passage from the blue to the green area), and then a sequence of period doubling bifurcations with the transition to chaos. Initially, there is a nonsymmetric chaotic attractor. Therefore, four attractors coexist here as symmetric partners with

respect to the symmetry operations S1 and S2. Next, they merge into a single symmetric chaotic attractor. When varying parameters inside the area occupied mostly by chaos, one observes narrow windows of periodicity. After leaving the region of complex dynamics, we reach the domain of periodic self-oscillations, marked as dark blue on the chart, and after that the black area of the stationary regime of steady fall. It should be noted that the boundary of these regions in the right part of the chart does not coincide with the curve of stability loss; this is due to a change in the nature of the Andronov – Hopf bifurcation (change from a supercritical bifurcation, accompanied by soft creation or disappearance of a limit cycle in the left part of the chart, to a subcritical bifurcation, corresponding to hard transition and hysteresis in the right part of the chart).

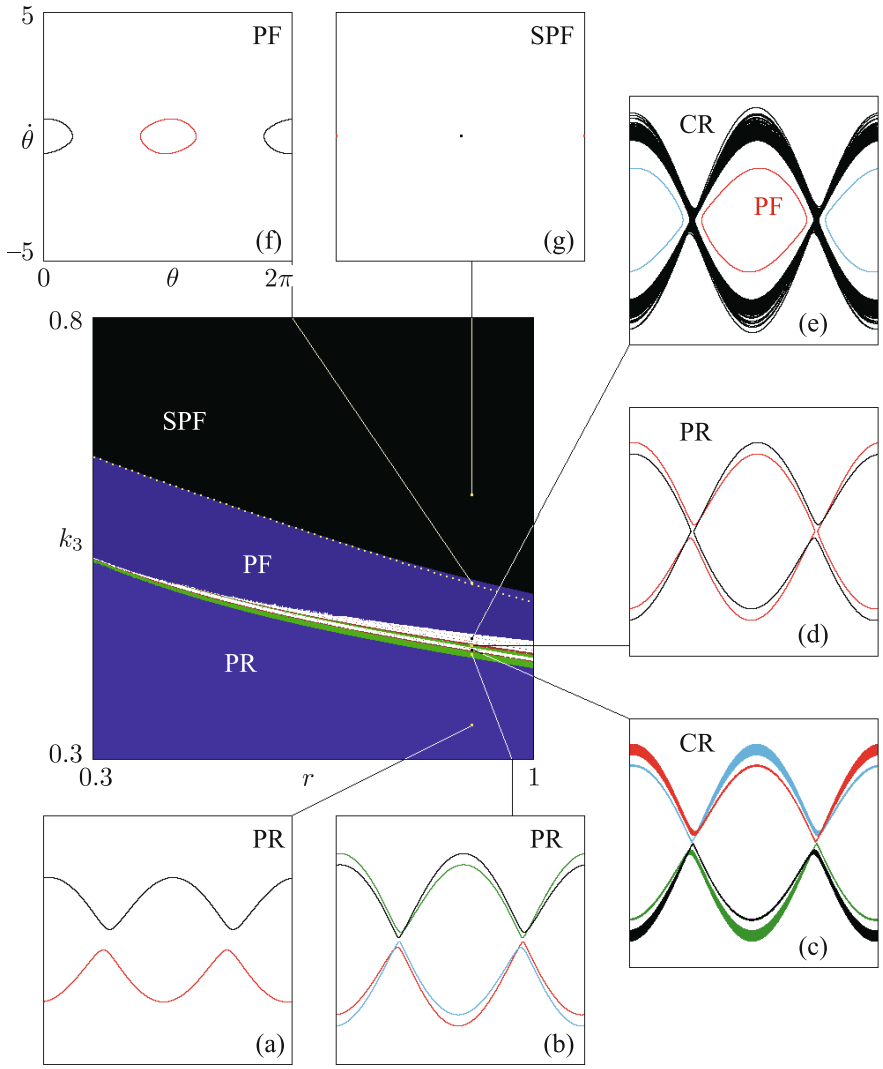

Fig. 19. Chart of regimes for the model (3.16) with fixed $k_1 = 0.06$ and $k_2 = 0.3$ obtained by scanning the parameter plane (r, k_3) upward with inheritance, and phase portraits of attractors as projected onto the plane $(\theta, \dot\theta)$ at representative points. The attractors that are symmetric partners with respect to S1 and S2 are shown in different colors. The domain PR corresponds to periodic autorotation, the domain PF corresponds to periodic oscillations (flutter), the domain SPF represents a fall without oscillations. The symbols CR and CF on the phase portraits indicate the chaotic regimes of rotation and flutter. The dotted line is the threshold of stability loss for the fixed point (3.17).

Figure 20 shows the phase portraits of attractors, which may be compared with those of the attractors of the Tanabe – Kaneko model in Fig. 13; observe the visually similar forms. The attractor in diagram (a) is the limit cycle arising after the symmetry breaking bifurcation and

two period doubling bifurcations. Diagram (b) shows a chaotic attractor formed as a result of a cascade of period doubling bifurcations. Since it is asymmetric, we can be sure that the symmetric partners coexist, which are generated by the symmetry operations S1 and S2. Diagram (c) shows a symmetric chaotic attractor, which may be interpreted as a result of unification of those symmetric partners into a single object. The Lyapunov exponents of the attractors calculated by solving the system (3.16) and the corresponding variation equations with the Benettin algorithm [14, 15, 18] are listed in the figure caption.

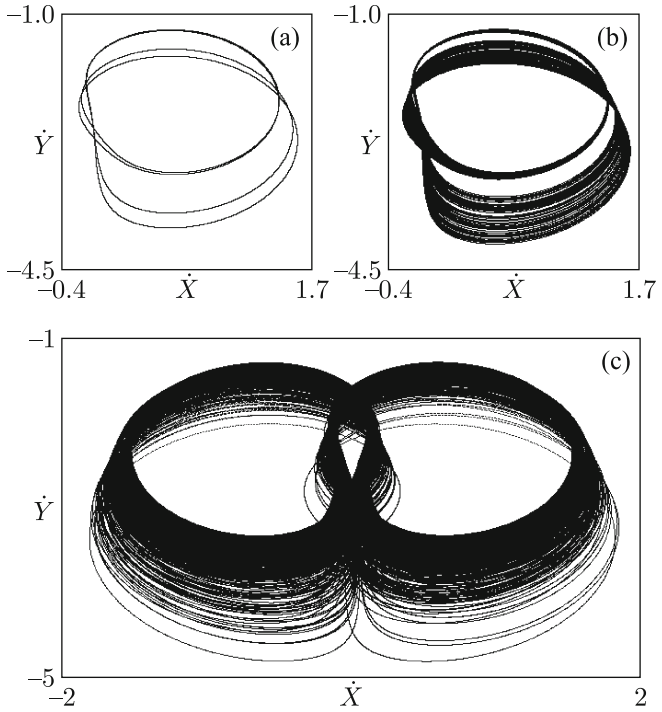

Fig. 20. Phase portraits of attractors for the Kozlov model (3.16) with $k_3 = 0.423$ (a), 0.424 (b), 0.437 (c). The other parameters are $r = 0.9$, $k_1 = 0.06$, $k_2 = 3$. The dimensionless components of the translational velocity in the laboratory frame are plotted along the coordinate axes: $\dot{X} = u\cos\theta - v\sin\theta$, $\dot{Y} = u\sin\theta + v\cos\theta$. The Lyapunov exponents are $\{0, -0.089, -0.326, -2.106\}$ (a), $\{0.091, 0, -0.326, -2.272\}$ (b), $\{0.186, 0, -0.341, -2.398\}$ (c).

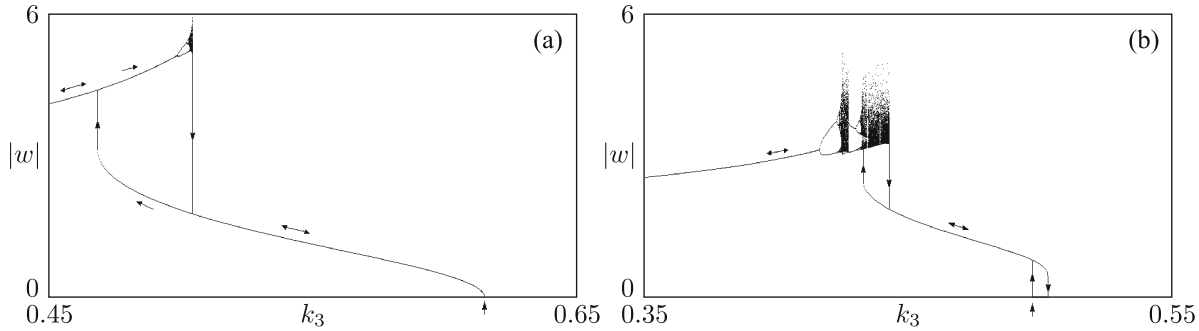

Fig. 21. One-parameter bifurcation diagrams obtained in computations for the Kozlov model (3.16) with $k_1 = 0.06$, $k_2 = 3$, $r = 0.4$ (a) and $r = 0.9$ (b). The directions of variation of the parameter are indicated by arrows at the branches of the diagrams. The vertical arrow indicates the point of stability loss for the steady fall according to (3.17).

To visualize multistability, let us turn to a one-parameter bifurcation diagram. In Fig. 21, the absolute value of the angular velocity is plotted versus the parameter of viscous friction for the

rotational motion. In computations this parameter k_3 is increased (decreased) step by step, the initial conditions used each time correspond to the final state at the previous step. The branches obtained by scanning from left to right and from right to left are indicated with arrows. The difference between the regimes observed in both cases indicates the presence of distinct coexisting attractors for the same parameters, each of which has its own basin in the state space (a set of initial starting points which the phase trajectories leave to arrive finally at this attractor). This is the hysteresis effect.[4)]

Diagram (a) demonstrates a single region of bistability, where one of the coexisting attractors is a limit cycle corresponding to periodic flutter, and the second corresponds to periodic (in the left part of the interval) or chaotic (in the right part of the interval) autorotation. The bifurcation of the birth of limit cycles, which is a normal (supercritical) Andronov – Hopf bifurcation, occurs at the point marked with the arrow below the horizontal axis.

Diagram (b) shows two parameter intervals of bistability. In one of them, on the left side of the figure, attractors coexist which are associated with periodic flutter (lower branch) and with chaotic autorotation (upper branch). In the second interval of bistability a limit cycle corresponding to periodic self-oscillations coexists with a stable fixed point corresponding to a steady fall. Here the Andronov – Hopf bifurcation of stability loss of the fixed point marked with the arrow is subcritical [19, 44, 45].

8.3. Modified Tanabe – Kaneko Model

The modification of the Tanabe – Kaneko model discussed in Section 8.1 leads to the equations

$$\begin{aligned} &\dot u = v\dot\theta + 2rv^2\operatorname{sgn} u - \sin\theta - rk_1u,\\ &(1+r)\dot v = (r-1)u\dot\theta - 2ruv\operatorname{sgn} u - \cos\theta - rk_2v,\\ &\left(\frac14+\frac18 r\right)\ddot\theta = -ruv - rk_3\dot\theta. \end{aligned} \tag{8.12}$$

Choosing an appropriate value of r, it is possible to achieve rather a good agreement of the dynamics in the modified and the original equations ((8.12) and (5.1), respectively).[5)]

Figure 22 shows a chart of regimes of the model (8.12) in the parameter plane (k_2, $f = k_2/k_1$) at $k_3 = k_2/4$ and $r = 0.1$. It can be compared with the chart of the original system of Tanabe – Kaneko in Fig. 11. As is seen, the charts look very similar. (The scales of the figures are chosen to make clear the visual comparison, although Eqs. (8.12) and (5.1) have been rescaled differently.) In both versions of the model, there are similar regimes, and there is an obvious correspondence between the relative positions of domains of different regimes in the parameter plane. Figure 23 shows the phase portraits of the attractors for the model (8.12) at $f = k_2/k_1 = 100$, $k_3 = k_2/4$ for a number of values k_2, which look similar to the attractors of the original model in Fig. 13.

Bearing in mind the subsequent comparison with the Anderson – Pesavento – Wang model, we consider the chart of regimes in the parameter plane (r, k_3) for fixed k_1 and k_2. The chart shown in Fig. 24 was obtained by scanning upward with inheritance. On the periphery of the figure the phase portraits of attractors are shown, and those coexisting at identical parameters are drawn in different colors.

Moving upward in the parameter plane (i. e., increasing the dissipation parameter), on the left side of the chart we first observe a bifurcation of symmetry breaking of the autorotation (transition

[4)] We emphasize that the attractors coexisting here are not symmetric partners with respect to the symmetry operations S1 and S2.

[5)] After the change of variables and parameters $v_x = u\sqrt{2gl/3}$, $v_y = v\sqrt{2gl/3}$, $t = \tau\sqrt{2l/3g}$, $rk_1 = k_\parallel\sqrt{2l/3g}$, $rk_2 = k_\perp\sqrt{2l/3g}$, $4rk_3 = k_\perp\sqrt{2l/3g}$, Eqs. (5.1) reduce to the form $\dot u + k_1u = \dot\theta v - \sin\theta + \frac23\pi\overline\rho lv\operatorname{sgn} u$, $\dot v + k_2v = -\dot\theta u - \cos\theta - \frac23\pi\overline\rho luv\operatorname{sgn} u$, $\ddot\theta + k_3\dot\theta = -\frac43\pi\overline\rho luv$. If we assume that $r = \frac13\pi\overline\rho l$ and take parameters as those in [23], it gives $r \approx 0.1$, and the above expressions are very similar to (8.12), with the only difference in the nearly unity coefficients $1+r$, $1-r$, $1+r/2$. Therefore, the dynamics of models (5.1) and (8.12) are similar, which is observed in the computations.

from the blue to the green region), then a sequence of period doubling bifurcations follows with a transition to chaos. Initially, an asymmetric chaotic attractor arises along with symmetric partners with respect to the S1 and S2 symmetries. With further parameter increase they merge into a single symmetric chaotic attractor. Inside the complex dynamics domain occupied mostly by chaos, narrow windows of periodicity occur which can correspond either to flutter or to autorotation.

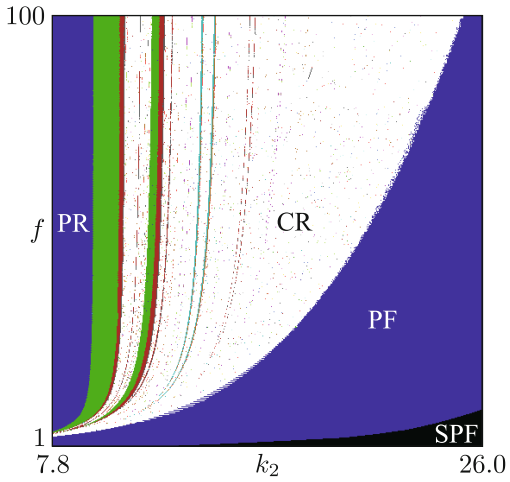

Fig. 22. Chart of regimes of the modified Tanabe – Kaneko model (8.12) for $r = 0.1$ at $k_1 = k_2/f$, $k_3 = k_2/4$ on the parameter plane (k_2, f). The colors are determined by a repetition period for the squared angular velocity in the Poincaré section. Period-1 regimes with and without symmetry are shown in blue and green, respectively; the other colors correspond to larger periods. The white areas represent chaos or unrecognized high-period regimes. The inscriptions denote periodic rotation (PR), chaotic rotation (CR), and periodic flutter (PF). Black denotes a simple perpendicular fall (SPF).

In the right part of the chart, the exit from the area of periodic dynamics upward is accompanied by a rigid transition and hysteresis. In particular, at the point (0.95, 0.1) periodic regimes of autorotation and flutter coexist. When moving in the parameter plane in the opposite direction (from the top down), we observe initially the periodic oscillations (flutter), which correspond to a limit cycle of the first kind (dark blue area in the upper right corner of the chart). Gradually, the limit cycle increases in size and at some place, obviously due to the approach to the saddle, its topological nature is changing, and it turns into a limit cycle of the second kind corresponding to autorotation (the area indicated in lighter blue). Then this cycle loses symmetry (transition from the blue to the green region), and after that the cascade of period doubling bifurcations for autorotation regimes occurs with transition to the chaotic tumbling regime.

8.4. Modified Belmonte – Eisenberg – Moses Model

The equations for the modified Belmonte – Eisenberg – Moses model read

$$\begin{aligned} \dot{u} &= v\dot{\theta} + 2rv^2 \operatorname{sgn} u - \sin\theta - \alpha_{\parallel} r\sqrt{u^2+v^2}\,u, \\ (1+r)\dot{v} &= (r-u)\dot{\theta} - 2ruv \operatorname{sgn} u - \cos\theta - \alpha_{\perp} r\sqrt{u^2+v^2}\,v, \\ \left(\frac{1}{4}+\frac{1}{8}r\right)\ddot{\theta} &= -ruv - \alpha_{\omega} r|\dot{\theta}|\dot{\theta}. \end{aligned} \tag{8.13}$$

Figure 25 shows a chart of regimes for the system (8.13) in the parameter plane (r, α_{ω}) obtained by scanning from left to right with inheritance. On the periphery, the portraits of attractors are shown as projected onto the plane $(\theta, \dot{\theta})$ at some representative points. The attractors coexisting at identical parameters are drawn in different colors. The inscriptions on the map are explained in the caption and correspond to the nomenclature of Tanabe and Kaneko.

The attractors for regimes of periodic flutter PF and periodic autorotation PR exhibit a visual similarity with the portraits in Fig. 16. However, a quantitative comparison of the modified

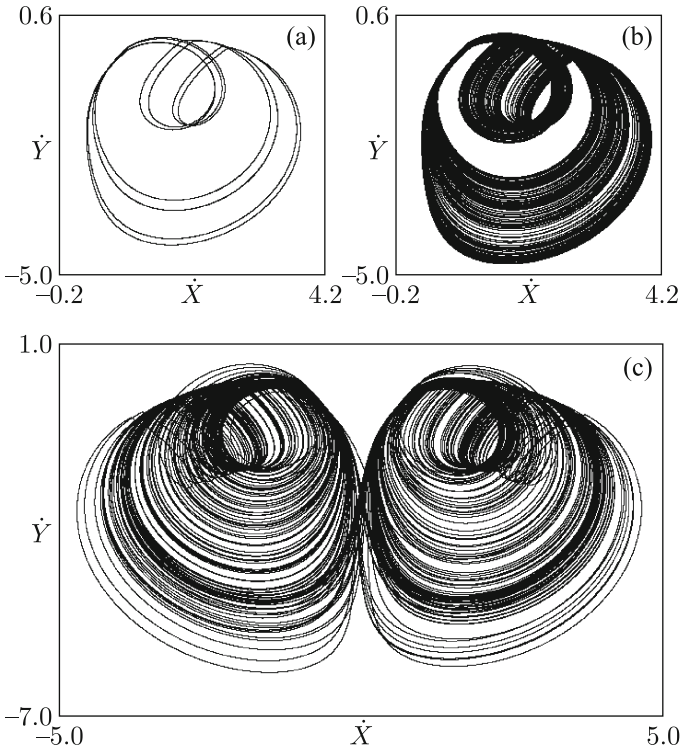

Fig. 23. Phase portraits of attractors of the model (8.12) with $k_2 = 10.86$ (a), 11 (b), 11.6 (c), $k_1 = k_2/100$ for $r = 0.1$. Dimensionless velocity components in the laboratory frame are plotted along the coordinate axes. The Lyapunov exponents are: {0, −0.029, −0.359, −1.906} (a), {0.043, 0, −0.435, −1.862} (b), {0.098, 0, −0.488, −1.757} (c).

model (8.13) with the original Belmonte – Eisenberg – Moses model (6.4) does not appear legitimate. As can be shown, the Froude number determined according to [26] and expressed in terms of parameters of the model (8.13) is $\mathrm{Fr} = \sqrt{\pi/r}$, so at parameters used in Figs. 15 and 16 the Froude numbers 0.89 and 0.45 correspond to large values of r (about 4 and 15). This corresponds to a very significant contribution of added masses, which are not taken into account in Eqs. (6.4).

8.5. Anderson – Pesavento – Wang Model as Compared with Others

As noted, the Anderson – Pesavento – Wang model [28] is the most elaborated finite-dimensional model for description of the fall of a plate in a resisting medium. Using the rescaled variables and parameters introduced in this section, Eqs. (7.3) can be rewritten as

$$\begin{gathered}
\dot{u} = (1-r)v\dot{\theta} - \frac{2ru^3}{5\pi\sqrt{u^2+v^2}} - \sin\theta, \\
(1+r)\dot{v} = (2r-1)u\dot{\theta} - r\frac{14u^2+12v^2}{5\pi\sqrt{u^2+v^2}}v - \cos\theta, \\
\left(\frac{1}{4}+\frac{1}{8}r\right)\ddot{\theta} = -ruv - r\left(\mu_1+\mu_2|\dot{\theta}|\right)\dot{\theta},
\end{gathered} \tag{8.14}$$

where $r = 1/I^*$. Bearing in mind the comparison with other models, it is natural to study the dynamics depending on the parameters that appear both in (8.14) and in the models to be compared. In this connection, we use r as one variable parameter, and the coefficient of linear or quadratic force resisting rotation in the third equation as another one. As for the first two equations, their form and coefficients will be assumed to be constant.

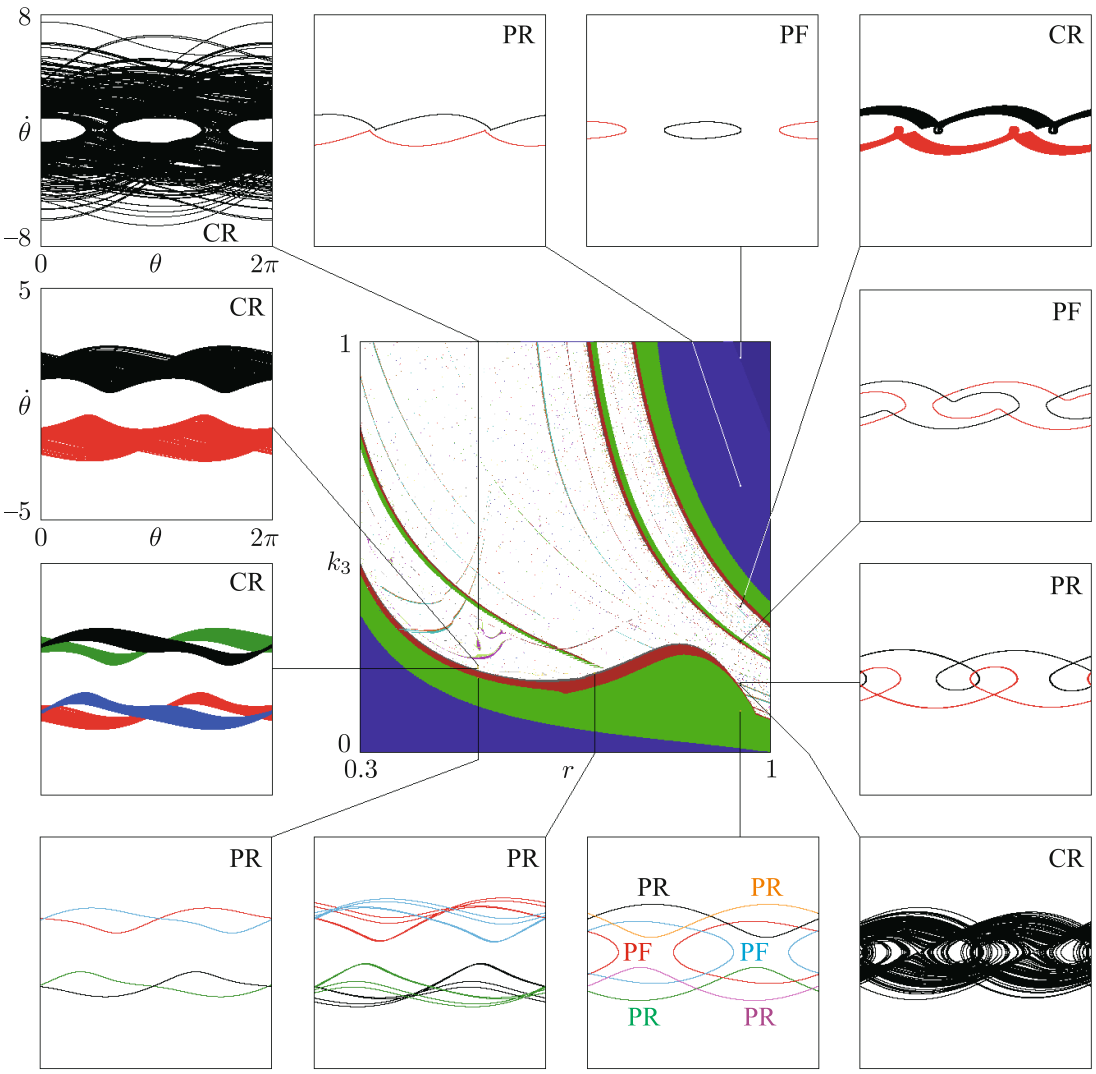

Fig. 24. Chart of regimes for the modified Tanabe – Kaneko model (8.12) on the parameter plane (r, k_3) with $k_1 = 0.06$, $k_2 = 3$. On the periphery the portraits of attractors are shown at representative points corresponding to periodic rotation PR, chaotic rotation CR, periodic flutter PF, and chaotic flutter CF. The colors are determined by a repetition period for the squared angular velocity in the Poincaré section. Period-1 regimes with and without symmetry are shown in blue and green, respectively. The other colors correspond to larger periods. The white areas represent chaos or unrecognized high-period regimes.

With the above rescaling, the loss of stability for a steady fall occurs at the critical coefficient of friction

$$\mu_1 = \mu_* = \frac{1}{4}\sqrt{\frac{3}{5\pi r}}\,\frac{2+r}{1-r}. \tag{8.15}$$

Figure 27 shows a chart of regimes on the plane of viscous friction coefficient μ_1 and parameter r in the absence of the quadratic resistance force for rotation ($\mu_2 = 0$). Figure 28 provides a chart on the plane of the quadratic friction coefficient μ_2 and the parameter r without rotational viscous friction ($\mu_1 = 0$). Both charts are obtained by scanning upward with inheritance. The inscriptions on the charts and portraits of attractors follow the nomenclature of Tanabe and Kaneko: PR and CR denote, respectively, periodic and chaotic autorotation, PF means periodic flutter oscillations, SPF is a simple perpendicular fall of the plate without oscillations. On the periphery of the figure the phase portraits of attractors are shown.

The chart in Fig. 27 is appropriate for comparison of the results with the Kozlov and Tanabe – Kaneko models, and the chart in Fig. 28 is suitable for comparison with the model of Belmonte, Eisenberg and Moses.

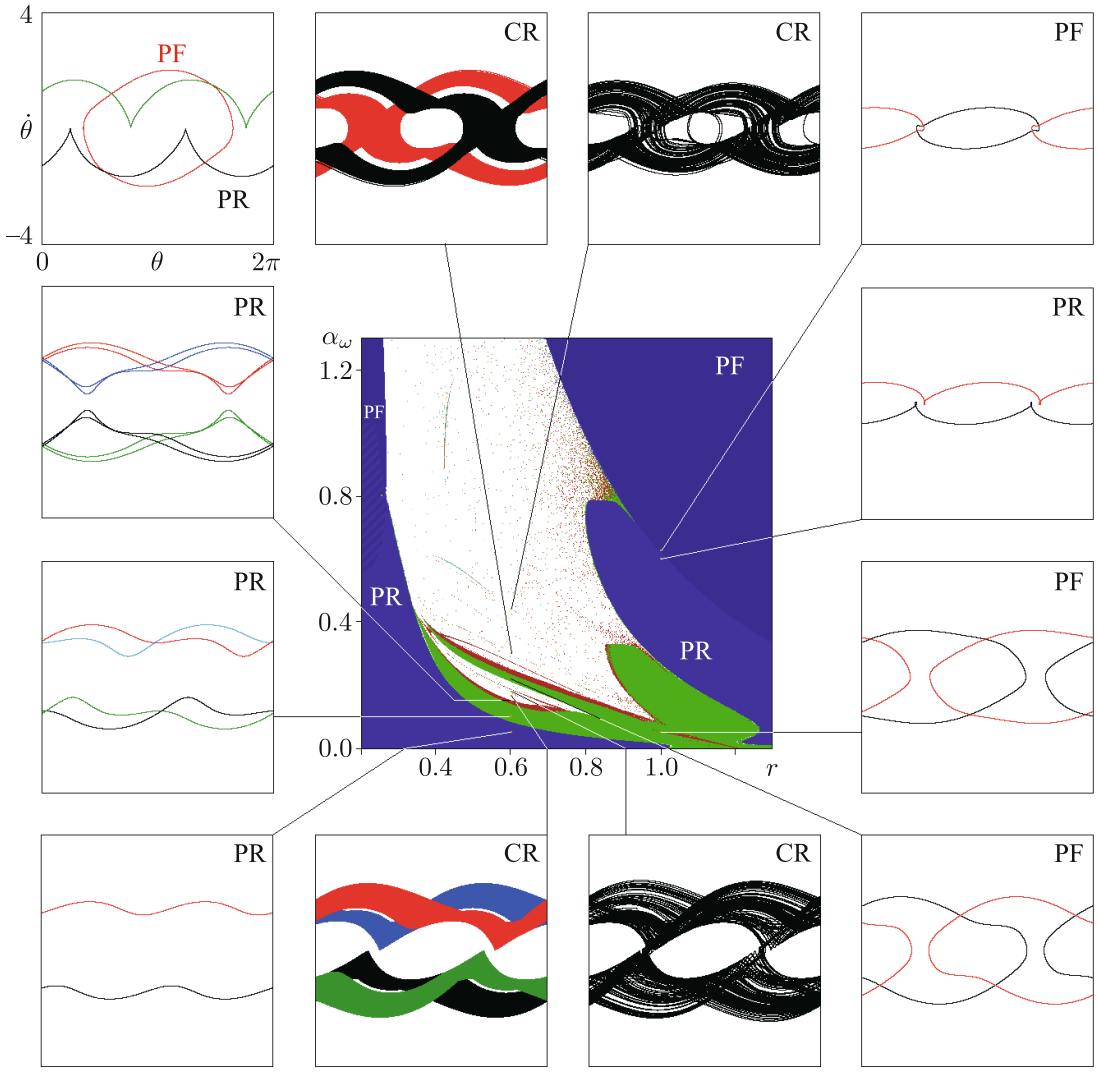

Fig. 25. Chart of regimes for the model (8.13) with $\alpha_\parallel = 0.14$, $\alpha_\perp = 0.65$ and phase portraits of attractors as projected onto the plane $(\theta, \dot\theta)$ at representative points corresponding to periodic rotation PR, chaotic rotation CR, periodic flutter PF, and chaotic flutter CF. The colors are determined by a repetition period for the squared angular velocity in the Poincaré section. Period-1 regimes with and without symmetry are shown in blue and green, respectively. The other colors correspond to larger periods. The white areas represent chaos or unrecognized high-period regimes.

In addition to the Anderson – Pesavento – Wang model, it is interesting to consider its approximate version, using circulation and resistance forces under the assumption that the longitudinal translational motion of the plate is characterized by a much greater velocity than the orthogonal component. In the limit case $|u| \gg |v|$ the circulation is given by the expression

$$\overline{\Gamma} = -\frac{12}{5\pi}\operatorname{sgn} u + 2\dot\theta = -0.76\operatorname{sgn} u + 2\dot\theta. \tag{8.16}$$

It is similar in structure to the formula (8.9) from the book of Sedov [9] based on the Kutta – Joukovsky – Chaplygin postulate used in the modified Tanabe – Kaneko and Belmonte – Eisenberg – Moses models (8.12) and (8.13). Note, however, a difference in the numerical coefficients: instead of 2 and 1 in (8.9) the expression (8.16) contains the constants 0.76 and 2.

The resistance force coefficients for the translational motion are expressed in this approximation as

$$K_{x,y} = \frac{2}{5\pi}\sqrt{u^2+v^2} = 0.13\sqrt{u^2+v^2}, \tag{8.17}$$

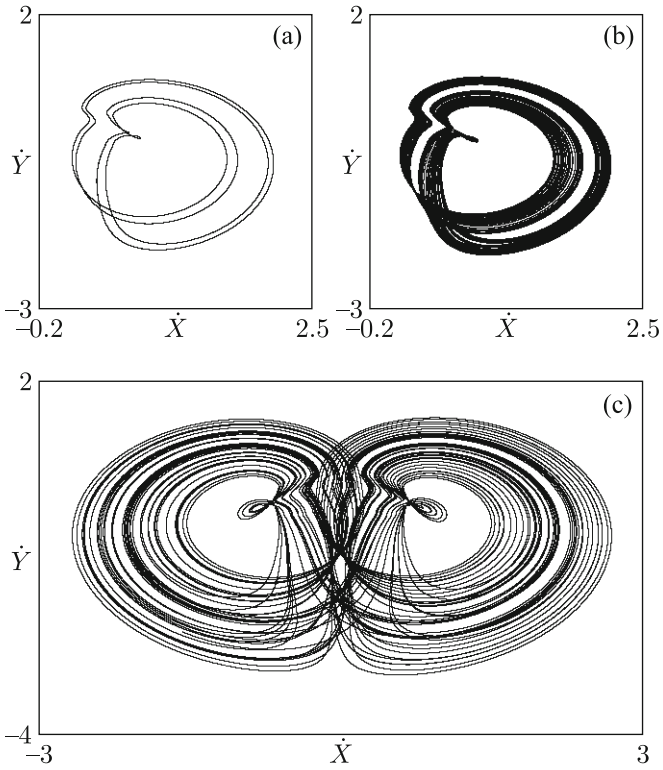

Fig. 26. Phase portraits of attractors for the model (8.13) with $r = 0.6$ and $a_w = 0.157$ (a), 0.16 (b), 0.2 (c). Dimensionless components of the translational velocity in the laboratory frame $\dot{X} = u\cos\theta - v\sin\theta$, $\dot{Y} = u\sin\theta + v\cos\theta$ are plotted along the coordinate axes. The Lyapunov exponents are {0, −0.042, −0.337, −1.493} (a), {0.037, 0, −0.414, −1.516} (b), {0.133, 0, −0.526, −1.726} (c).

which differs from the Belmonte – Eisenberg – Moses model in the numeric constants. (Instead of 0.14 and 0.65 for the longitudinal and transversal motion we have the same coefficient 0.13.)

The dynamical equations for this limit case of the Andersen – Pesavento – Wang model may be written as

$$\begin{aligned} \dot{u} &= (1-r)v\dot{\theta} - \frac{2}{5\pi}ru^2\operatorname{sgn} u - \sin\theta, \\ (1+r)\dot{v}_y &= (2r-1)u\dot{\theta} - \frac{14}{5\pi}ruv\operatorname{sgn} u - \cos\theta, \\ \left(\frac{1}{4}+\frac{1}{8}r\right)\ddot{\theta} &= -ruv - r\left(\mu_1' + \mu_2|\dot{\theta}|\right)\dot{\theta}. \end{aligned} \tag{8.18}$$

Figure 29 shows the chart of regimes in the plane of parameter r and the coefficient of viscous friction for rotational motion of the body μ_1. Panel (a) corresponds to the Anderson – Pesavento – Wang model (8.14), and (b) to the approximate version of this model (8.18). Panel (c) relates to the modified Tanabe – Kaneko model (8.12).

Figure 30 shows the chart of regimes in the plane of parameter r and the factor of quadratic resistance force for rotational motion; the viscous friction is absent ($\mu_1 = 0$). As in the previous figure, panels (a) and (b) refer to the Anderson – Pesavento – Wang model (8.14) and to the limit case of this model (8.18). Panel (c) corresponds to the modified Belmonte – Eisenberg – Moses model (8.13).

Comparing panels (a) and (b) in Figs. 29 and 30, one observes that the general structure of the regions in the parameter space is analogous, although the relative size and the relative positions of the formations vary. This observation motivates the use of the circulation formula within the Kutta – Joukovsky – Chaplygin postulate at least at the level of qualitative analysis.

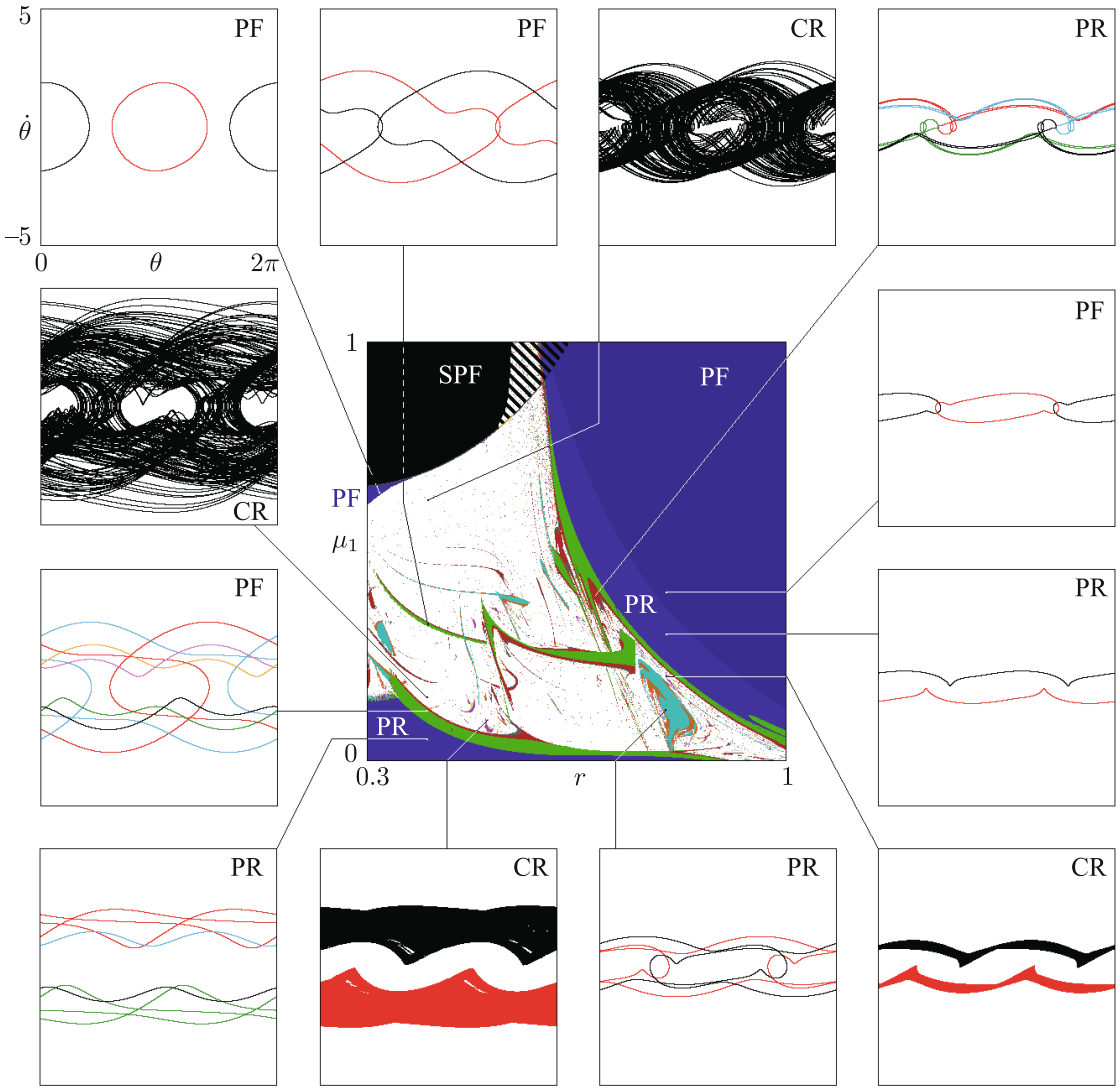

Fig. 27. Chart of regimes for the model (8.14) with $\mu_2 = 0$, obtained by upward scanning with inheritance, and phase portraits of attractors at representative points. The attractors coexisting at identical parameters are shown in different colors. PR means periodic autorotation, PF periodic flutter, SPF a steady perpendicular fall. The inscriptions CR and CF relate to chaotic regimes of rotation and flutter. The inclined stripes on the right side of the SPF area denote the region of coexistence of autorotation or flutter regimes with the steady fall.

Less striking, but noticeable, similarities are seen between diagrams (b) and (c) in both figures. The presence of regions PF in the upper right corner of the charts and the presence of PR in the lower left corner are observed, while chaotic dynamics are observed in the central part of the charts. Another common feature is the transition to chaos through the period doubling cascade preceded by the symmetry breaking bifurcation in the bottom left part of the charts. Thus, despite some quantitative differences, the general picture of dynamics that results from the models considered looks quite recognizable and consistent. Obviously, this is due to common underlying conservative dynamics (Kirchhoff equations), common symmetry properties, and the universal nature of the phenomena involved in nonlinear dynamics (fixed points, limit cycles, attractors, and bifurcations).

CONCLUSION

The article reproduces results of studies of the plane problem of a plate falling in a resisting medium based on models in the form of ordinary differential equations for a relatively small number of variables, and provides a comparative analysis of these models. The methodological basis for the

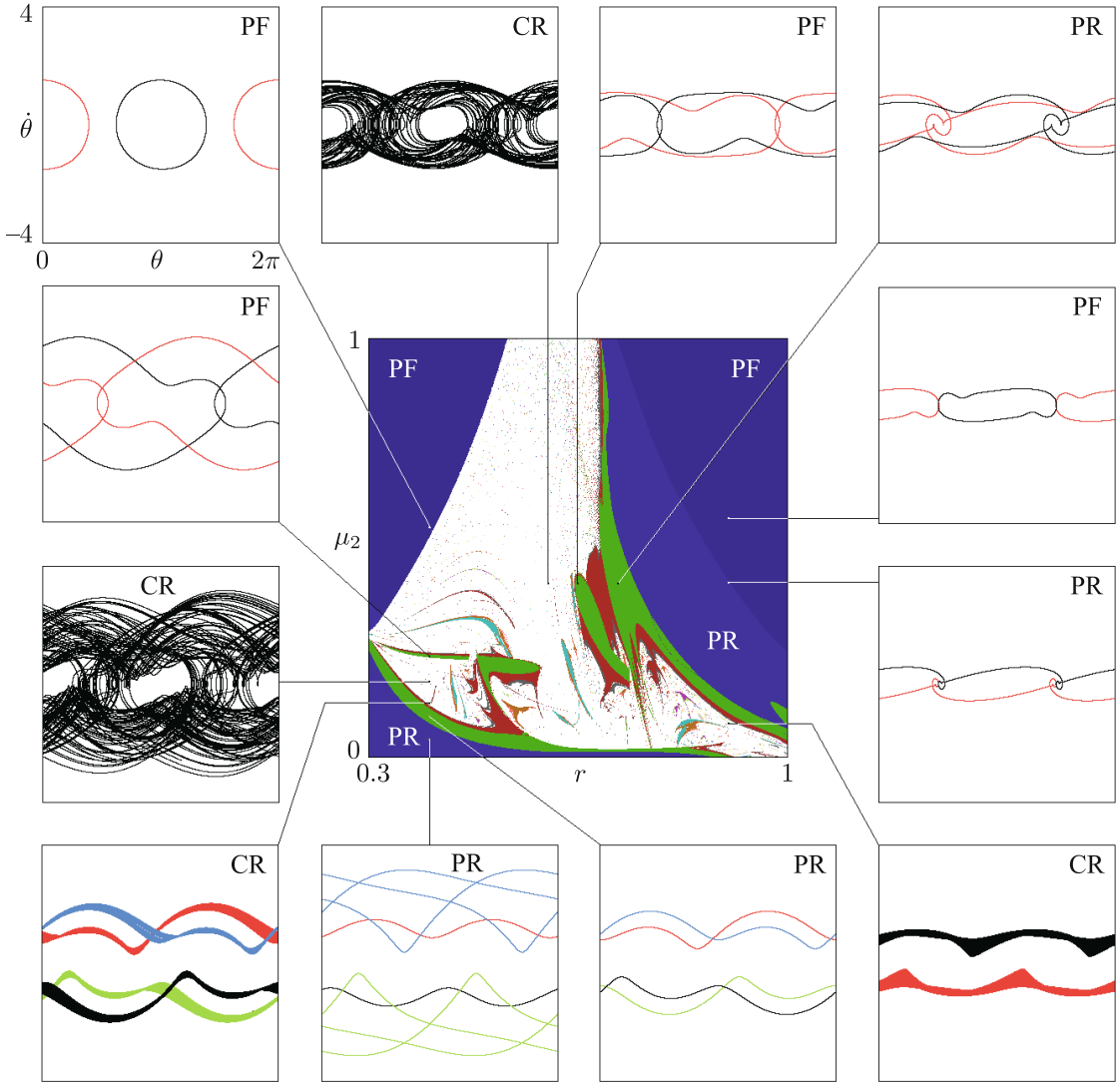

Fig. 28. Chart of regimes for the model (8.14) with $\mu_1 = 0$, obtained by scanning the parameter plane (r, μ_2) upward with inheritance, and phase portraits of attractors at representative points. The notation and inscriptions are similar to those used in the previous figure.

finite-dimensional description is the fact that in the case of an ideal incompressible nonviscous fluid the generalized coordinates and velocities of the rigid body are governed by the Kirchhoff equations decoupled from the fluid dynamics equations.

As part of the review we tried to draw a line of reasoning, starting from a situation where the Kirchhoff equations are reduced to the pendulum equation with sine nonlinearity to models showing self-oscillatory and rotational periodic or chaotic regimes by taking into account certain assumptions concerning forces acting on the body from the viscous medium. Such an approach proves to be fruitful in the general theory of oscillations, when a conservative oscillator is used as a starting model for subsequent modifications involving the damping of oscillations, excitation of self-oscillations, and the occurrence of chaotic dynamics.

In the problem of a body falling in a resisting medium, the periodic oscillations (flutter) and periodic motion with tumbling (autorotation) are interpreted as those associated with the limit cycles of the first and second kind in the phase space (more precisely, in the subspace of the generalized velocities).

To study the problem of a body falling in a fluid, we have applied concepts and tools of nonlinear dynamics, including visualization of the dynamical phenomena by means of the portraits

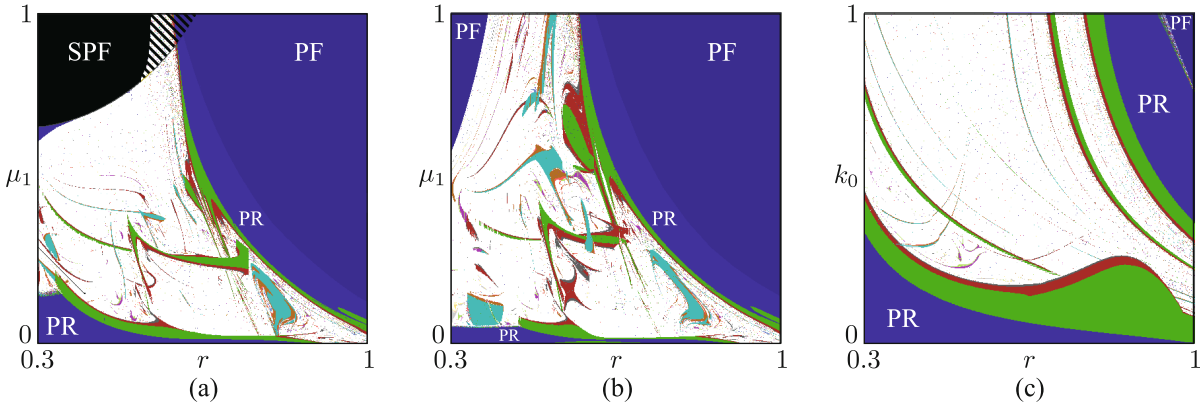

Fig. 29. Comparison of charts of regimes for the Andersen – Pesavento – Wang model (a), the limit case of this model (b), and for the modified Tanabe – Kaneko model (c).

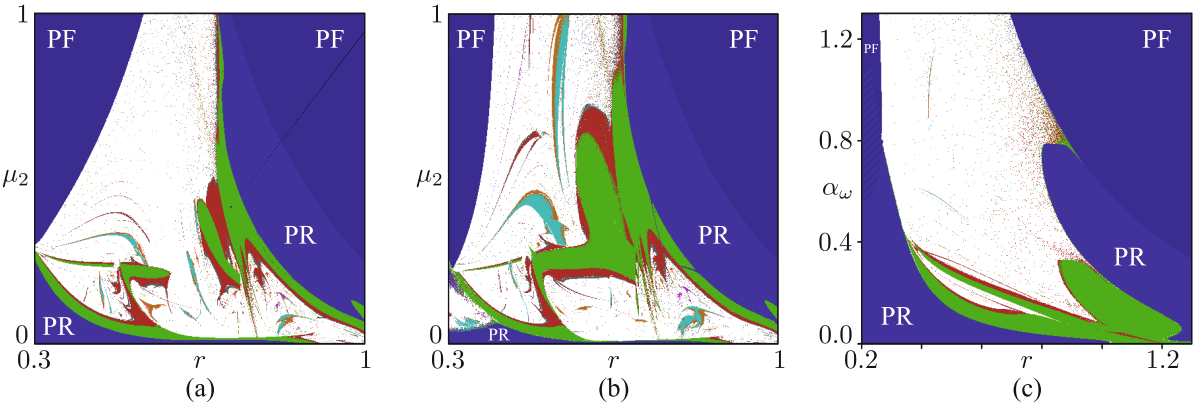

Fig. 30. Comparison of charts of regimes for the Andersen – Pesavento – Wang model (a), the limit case of this model (b), and for the modified Belmonte – Eisenberg – Moses model (c).

of attractors, analysis of Poincaré recurrence maps, mapping dynamical regimes in the parameter plane (charts of dynamical regimes), analysis of bifurcation diagrams ("trees"), and computation of the spectra of Lyapunov exponents. This has made it possible to flesh out the picture of the dynamics revealed by the finite-dimensional models using extensive illustrative material.

An unexpected richness of dynamical behavior deserving attention has been revealed using the simplest model [22], where only linear viscous resistance for translational and rotational motions of the body is taken into account, while circulation and related effects like the lift force are ignored. Previously, attention was focused only on simple regimes of the dynamics of this model, but in a certain parameter range rather complex phenomena such as chaos, cascade of period doubling bifurcations, multistability are possible.

An original result is the discovery of a Lorenz-type strange attractor in the three-dimensional space of generalized velocities for the problem of motion of a body with elliptic profile under the conditions of compensated gravity, in the presence of viscous friction, with constant velocity circulation around the profile, and with external constant torque applied to the body.

An analysis has been made concerning the Tanabe – Kaneko model, which takes into account the action of the lift force on the moving profile according to the Kutta – Joukovsky – Chaplygin postulate. This analysis includes reproduction of results of the original work, modification of the model taking into account the criticisms it was subjected to, and comparison of the original and the modified model. It reveals that, despite seemingly significant deficiencies, the model qualitatively gives a reasonable general picture of possible phenomena of complex dynamics for the fall of a plate in a fluid, at least in a certain range of parameters. A similar analysis has been made of the Belmonte – Eisenberg – Moses model assuming that the friction is quadratic in the generalized velocities.

For the Anderson – Pesavento – Wang model based on the proposed empirical formulas for the drag and lift forces, an extensive numerical material, including charts of regimes in the parameter space, has been presented.

We introduce a generalized model using common dimensionless variables and parameters and provide a comparative analysis of the dynamical behavior of the Kozlov, Tanabe – Kaneko, Belmonte – Eisenberg – Moses and Andersen – Pesavento – Wang models.

It is worth noting the important role of symmetry for the problem for understanding the inherent phenomenology of complex dynamics of a plate falling in a fluid. In particular, a relevant feature is the possibility of coexistence of attractors, which are mutually symmetrical objects, and the possibility of combining them into a single attractor under variation of control parameters.

We conclude that the overall structure of the parameter space for different models exhibits certain similarities. Thus, despite the quantitative difference, the picture drawn on the basis of the finite-dimensional models for a plate falling in a resisting medium appears to be quite consistent. This fact is determined, first, by common underlying conservative dynamics (Kirchhoff equations). Second, the modification of the equations taking into account the effects of viscosity gives rise to common features of the dynamics due to the inherent symmetry and to the universal nature of the phenomena involved in nonlinear dynamics (fixed points, limit cycles, attractors, and bifurcations).

ACKNOWLEDGMENTS

I would like to express thanks to A. V. Borisov who called my attention to the issues discussed in this paper.

This work was partially supported by a grant of the President of the Russian Federation for leading scientific schools NSH-1726.2014.2 “Fundamental problems of nonlinear dynamics and their applications” and RFBR grant 14-02-00085.

REFERENCES

1. Maxwell, J. K., On a Particular Case of Descent of a Heavy Body in a Resisting Medium, *Cambridge and Dublin Math. Journ.,* 1854, vol. 9, pp. 145–148.
2. Kirchhoff, G. R., Über die Bewegung eines Rotationskörpers in einer Flüssigkeit, *J. Reine Angew. Math.,* 1870, vol. 1870, no. 71, pp. 237–262.
3. Zhukovsky N. E. *Collected Works: Vol. 4,* Moscow: Gostekhizdat, 1949, pp. 5–34 (Russian).
4. Belmonte, A. and Moses, E., Flutter and Tumble in Fluids, *Physics World,* 1999, vol. 12, no. 4, pp. 21–25.
5. Finn, D. L., Falling Paper and Flying Business Cards, *SIAM News,* 2007, vol. 40, no. 4, 3 pp.
6. Ern, P., Risso, F., Fabre, D., and Magnaudet, J., Wake-Induced Oscillatory Paths of Bodies Freely Rising or Falling in Fluids, *Annu. Rev. Fluid Mech.,* 2012, vol. 44, pp. 97–121.
7. Lamb, H., *Hydrodynamics,* 6th ed., New York: Dover, 1945.
8. Borisov, A. V. and Mamaev, I. S., *Dynamics of a Rigid Body: Hamiltonian Methods, Integrability, Chaos,* 2nd ed., Izhevsk: Institute of Computer Science, 2005 (Russian).
9. Sedov, L. I., *Two-Dimensional Problems in Hydrodynamics and Aerodynamics,* New York: Wiley, 1965.
10. Kochin, N. E., Kibel, I. A., and Roze, N. V., *Theoretical Hydrodynamics,* New York: Wiley, 1964.
11. Birkhoff, G., *Hydrodynamics: A Study in Logic, Fact, and Similitude,* Princeton: Princeton Univ. Press, 1950.
12. Arzhanikov, N. S. and Sadekova, G. S., *Aerodynamics of Aircrafts,* Moscow: Vysshaja Shkola, 1983 (Russian).
13. *Strange Attractors,* Y. G. Sinai, L. P. Shil'nikov (Eds.), Moscow: Mir, 1981 (Russian).
14. Schuster, H. G. and Just, W., *Deterministic Chaos: An Introduction,* Weinheim: Wiley-VCH, 2005.
15. Kuznetsov, S. P., *Dynamical Chaos,* 2nd ed., Moscow: Fizmatlit, 2006 (Russian).
16. Kuznetsov, A. P., Kuznetsov, S. P., Sataev, I. R., and Chua, L. O., Multi-Parameter Criticality in Chua's Circuit at Period-Doubling Transition to Chaos, *Internat. J. Bifur. Chaos Appl. Sci. Engrg.,* 1996, vol. 6, no. 1, pp. 119–148.
17. Borisov, A. V., Jalnin, A. Yu., Kuznetsov, S. P., Sataev, I. R., and Sedova, J. V., Dynamical Phenomena Occurring due to Phase Volume Compression in Nonholonomic Model of the Rattleback, *Regul. Chaotic Dyn.,* 2012, vol. 17, no. 6, pp. 512–532.
18. Benettin, G., Galgani, L., Giorgilli, A., and Strelcyn, J.-M., Lyapunov Characteristic Exponents for Smooth Dynamical Systems and for Hamiltonian Systems: A Method for Computing All of Them, *Meccanica,* 1980, vol. 15, pp. 9–30.

19. Kuznetsov, Yu. A., *Elements of Applied Bifurcation Theory,* 3rd ed., Appl. Math. Sci., vol. 112, New York: Springer, 2004.
20. Borisov, A. V., Kozlov, V. V., Mamaev, I. S., Asymptotic stability and associated problems of dynamics of falling rigid body, *Regul. Chaotic Dyn.*, 2007, vol. 12, no. 5, pp. 531–565.
21. Borisov, A. V. and Mamaev, I. S., On the Motion of a Heavy Rigid Body in an Ideal Fluid with Circulation, *Chaos,* 2006, vol. 16, no. 1, 013118, 7 pp.
22. Kozlov, V. V., On the Problem of Fall of a Rigid Body in a Resisting Medium, *Mosc. Univ. Mech. Bull.,* 1990, vol. 45, no. 1, pp. 30–36; see also: *Vestn. Mosk. Univ. Ser. 1. Mat. Mekh.,* 1990, no. 1, pp. 79–86.
23. Tanabe, Y. and Kaneko, K., Behavior of a Falling Paper, *Phys. Rev. Lett.,* 1994, vol. 73, no. 10, pp. 1372–1375.
24. Mahadevan, L., Aref, H., and Jones, S. W., Comment on ¡¡Behavior of a Falling Paper¿¿, *Phys. Rev. Lett.,* 1995, vol. 75, no. 7, p. 1420.
25. Tanabe, Y. and Kaneko, K., Tanabe and Kaneko Reply, *Phys. Rev. Lett.,* 1995, vol. 75, no. 7, p. 1421.
26. Mahadevan, L., Tumbling of a Falling Card, *C. R. Acad. Sci. Paris, Sér. 2b,* 1996, vol. 323, pp. 729–736.
27. Belmonte, A., Eisenberg, H., and Moses, E., From Flutter to Tumble: Inertial Drag and Froude Similarity in Falling Paper, *Phys. Rev. Lett.,* 1998, vol. 81, no. 2, pp. 345–348.
28. Andersen, A., Pesavento, U., and Wang, Z. J., Analysis of Transitions between Fluttering, Tumbling and Steady Descent of Falling Cards, *J. Fluid Mech.,* 2005, vol. 541, pp. 91–104.
29. Pesavento, U. and Wang, Z. J., Falling Paper: Navier – Stokes Solutions, Model of Fluid Forces, and Center of Mass Elevation, *Phys. Rev. Lett.,* 2004, vol. 93, no. 14, 144501, 4 pp.
30. Andersen, A., Pesavento, U., and Wang, Z. J., Unsteady Aerodynamics of Fluttering and Tumbling Plates, *J. Fluid Mech.,* 2005, vol. 541, pp. 65–90.
31. Noor, D. Z., Chern, M. J., and Horng, T. L., Study of a Freely Falling Ellipse with a Variety of Aspect Ratios and Initial Angles, in *Proc. of the 22nd Internat. Conf. on Parallel Computational Fluid Dynamics,* http://www1.math.fcu.edu.tw/~tlhorng/paper/Extended_abstract.pdf (2010).
32. Caetano, V. F. R., Calculation of the Dynamic Behavior of a Falling Plate or Disk in a Fluid, https://fenix.tecnico.ulisboa.pt/downloadFile/395142133553/resumo.pdf (2010).
33. Dupleich, P., Rotation in Free Fall of Rectangular Wings of Elongated Shape, http://digital.library.unt.edu/ark:/67531/metadc64688/ (1949, UNT Digital Library).
34. Huang, W., Liu, H., Wang, F., Wu, J., and Zhang, H. P., Experimental Study of a Freely Falling Plate with an Inhomogeneous Mass Distribution, *Phys. Rev. E.,* 2013, vol. 88, no. 5, 053008, 7 pp.
35. Mahadevan, L., Ryu, W. S., and Samuel, A. D. T., Tumbling Cards, *Phys. Fluids,* 1999, vol. 11, no. 1, pp. 1–3.
36. Field, S. B., Klaus, M., Moore, M. G., and Nori, F., Chaotic Dynamics of Falling Disks, *Nature,* 1997, vol. 388, no. 6639, pp. 252–254.
37. Heisinger, L., Newton, P., and Kanso, E., Coins Falling in Water, *J. Fluid Mech.,* 2014, vol. 742, pp. 243–253.
38. Leweke, T., Thompson, M. C., and Hourigan, K., Motion of a Möbius Band in Free Fall, *J. Fluids Struct.,* 2009, vol. 25, no. 4, pp. 687–696.
39. Lugt, H. J., Autorotation, *Annu. Rev. Fluid Mech.,* 1983, vol. 15, no. 1, pp. 123–147.
40. Paoletti, P. and Mahadevan, L., Planar Controlled Gliding, Tumbling and Descent, *J. Fluid Mech.,* 2011, vol. 689, pp. 489–516.
41. Ramodanov, S. M. and Tenenev, V. A., Motion of a Body with Variable Distribution of Mass in a Boundless Viscous Liquid, *Nelin. Dinam.,* 2011, vol. 7, no. 3, pp. 635–647 (Russian).
42. Fernandes, A. C. and Sefat, S. M., Bifurcation from Fluttering to Autorotation of a Hinged Vertical Flat Plate Submitted to a Uniform Current, in *Proc. of the 11th Internat. Conf. on the Stability of Ships and Ocean Vehicles (23-28 September 2012, Athens, Greece),* pp. 1–12.
43. Michelin, S. and Smith, S. G. L., Falling Cards and Flapping Flags: Understanding Fluid – Solid Interactions Using an Unsteady Point Vortex Model, *Theor. Comp. Fluid Dyn.,* 2010, vol. 24, nos. 1–4, pp. 195–200.
44. Andronov, A. A., Vitt, A. A., and Khaikin, S. E., *Theory of Oscillators,* Oxford: Pergamon Press, 1966.
45. Butenin N. V., Neumark Yu. I., Fufaev N. A. *Introduction to the Theory of Nonlinear Oscillations,* 2nd ed., Moscow: Nauka, 1987 (Russian).
46. Lorenz E. N. Deterministic Nonperiodic Flow, *J. Atmospheric Sci.,* 1963, vol. 20, no. 2, pp. 130–141.
47. Sparrow, C., *The Lorenz Equations: Bifurcations, Chaos, and Strange Attractors,* New York: Springer, 1982.
48. Shilnikov, L., Mathematical Problems of Nonlinear Dynamics: A Tutorial, *J. Franklin Inst.,* 1997, vol. 334, no. 5, pp. 793–864.
49. Tucker, W., A Rigorous ODE Solver and Smale's 14th Problem, *Found. Comput. Math.,* 2002, vol. 2, no. 1, pp. 53–117.

50. Pikovskii, A. S., Rabinovich, M. I., and Trakhtengerts, V. Yu., Onset of Stochasticity in Decay Confinement of Parametric Instability, *JETP,* 1978, vol. 47, no. 4, pp. 715–719; see also: *Zh. Èksp. Teor. Fiz.,* 1978, vol. 74, no. 4, pp. 1366–1374.
51. Hénon, M., On the Numerical Computation of Poincaré Maps, *Phys. D,* 1982, vol. 5, pp. 412–414.
52. Swift, J. W. and Wiesenfeld, K., Suppression of Period Doubling in Symmetric Systems, *Phys. Rev. Lett.,* 1984, vol. 52, no. 9, pp. 705–708.
53. Magnus, K., Popp, K., and Sextro, W., *Schwingungen: Eine Einführung in die physikalischen Grundlagen und die theoretische Behandlung von Schwingungsproblemen,* Wiesbaden: Springer, 2008.
54. Feigenbaum, M. J., Quantitative Universality for a Class of Nonlinear Transformations, *J. Stat. Phys.,* 1978, vol. 19, no. 1, pp. 25–52.
55. Feigenbaum, M. J., Universal Behavior in Nonlinear Systems, *Phys. D,* 1983, vol. 7, nos. 1–3, pp. 16–39.
56. Borisov, A. V., Kazakov, A. O., Sataev, I. R., The Reversal and Chaotic Attractor in the Nonholonomic Model of Chaplygin's Top, *Regul. Chaotic Dyn.*, 2014, vol. 19, no. 6, pp. 718–733.
57. Kuznetsov, A. P., Migunova, N. A., Sataev, I. R., Sedova, Y. V., Turukina, L. V., From Chaos to Quasi-Periodicity, *Regul. Chaotic Dyn.*, 2015, vol. 20, no. 2, pp. 189–204.
58. Vetchanin E. V., Mamaev I. S., Tenenev V. A., The Self-propulsion of a Body with Moving Internal Masses in a Viscous Fluid, *Regul. Chaotic Dyn.*, 2013, vol. 18, nos. 1–2, pp. 100–117.
59. Sokolov S. V., Ramodanov S. M., Falling Motion of a Circular Cylinder Interacting Dynamically with a Point Vortex, *Regul. Chaotic Dyn.*, 2013, vol. 18, nos. 1–2, pp. 184–193.